Deep Sea Research Part I: Oceanographic Research Papers
Volume 68, October 2012, Pages 24–45
http://dx.doi.org/10.1016/j.dsr.2012.05.015

How does dynamical spatial variability impact 234Th-derived estimates of organic export?

L. Resplandy[a,*], A.P. Martin[a], F. Le Moigne[a], P. Martin[a, b], A. Aquilina[a], L. Mémery[c], M. Lévy[d], R. Sanders[a]

[a] National OceanographyCentre,EuropeanWay,Southampton,UK
[b] Woods HoleOceanographicInstitution,USA
[c] LEMAR, Brest,France
[d] LOCEAN, Paris,France

*: Corresponding author : laure.resplandy@locean-ipsl.upmc.fr

Abstract:

In this study we first evaluate the small-scale spatial variability of particulate export, using a set of synoptic thorium-234 activity observations sampled within a one-degree radius. These data show significant variability of surface thorium activity on scales of the order of 100 km (~270–550 dpm m-3). This patchiness of export potentially affects the robustness of point observations and our interpretation of them. Motivated by these observations we subsequently couple an explicit model of thorium-234 dynamics to a coupled physical–biogeochemical basin model capable of resolving these small-scales. The model supports the observations in displaying marked thorium variability on spatial scales of the order of 100 km and smaller, with highest values in the regions of large eddy kinetic energy and large primary productivity. The model is also used to quantify the impact of small-scale variability on export estimates. Our model shows that the primary source of error associated with the presence of small-scale spatial variability is related to the standard assumptions of steady state and non-steady state (>40% during bloom condition). The non-steady state method can misinterpret variations due to patchiness in thorium activity as temporal changes and lead to errors larger than those introduced by the simpler steady state approach. We show that the non-steady state approach could improve the flux estimates in some cases if the sampling was conducted in a Lagrangian framework. Undersampling the spatial variability results in further bias (>20%) that can be reduced when the sampling density is increased. Finally, errors due to the dynamical transport of thorium associated with small-scale structures are relatively low (<20%) except in regions of high eddy kinetic energy.

Keywords: Export;Mesoscale;Thorium 234;Spatial variability

1. Introduction

The magnitude and variability of the sinking particle flux are fundamental to understanding the total carbon distribution in the ocean and thus the ocean-atmosphere partitioning of carbon and global climate (Siegenthaler and Sarmiento, 1993). Ocean biology and biogeochemistry are strongly influenced by ocean physics, since dynamical transport and mixing redistribute nutrients and particles horizontally and vertically. Although numerous observational and modelling studies have demonstrated that ocean dynamics at the mesoscale (scales of the order of 100 km) and below introduce spatial and temporal heterogeneities in the nutrient distribution and primary production (see Lévy, 2008 for a review), very little is known about their impact on the downward export of the resulting particulate matter. These studies have shown that enhanced vertical motion, lateral stirring and restratification associated with small-scale physical features affect the local structure and dynamics of the planktonic ecosystem (Fielding et al., 2001, Martin et al., 2001, Martin 2003, Painter et al., 2010, d'Ovidio et al., 2010) and the carbon and nutrient exchanges between the ocean interior and the upper water column (Lévy et al., 2001, Allen et al., 2005, McGillicuddy et al., 2007, Lathuilliere et al., 2010, Karleskind et al., 2011). As the particulate export directly depends on primary production, ecosystem dynamics and ocean transport processes, it is also likely to be affected by small-scale physics.

Particle flux can be measured directly by intercepting sinking material in sediment traps (Buesseler et al., 2007, Lampitt et al., 2008), or indirectly using methods such as those based on biological rates (Boyd et al., 1999), budgets of nutrients, oxygen or radioisotopes (Jenkins, 1982, Sanders et al., 2005, Rutgers van der Loeff et al., 2006), or by underwater imaging of particulate matter (Bishop et al., 2004, Guidi et al., 2007). Both direct and indirect approaches have revealed preliminary evidence for small scale spatial variability in export. Sediment traps have captured episodic fluxes of particulate material associated with open-ocean eddies (Newton et al., 1994, Honjo et al., 1999, Beaulieu, 2002, Sweeney et al., 2003, Alonso-Gonzalez et al., 2010). The observation program POMME (Programme Ocean Multidisciplinaire Meso Echelle) showed that a large quantity of particulate organic matter in the northeast Atlantic is exported downward in spatially limited areas surroundings eddies (Guidi et al., 2007). Moreover, studies based on thorium-234 disequilibria reveal that particulate export varies spatially and temporally within eddies (Benitez Nelson 2007, 2008, Buesseler et al. 2008, Maïti et al. 2008). Finally, thorium-234 observations sampled in the

north Pacific as part of the Hawaii Ocean Time-series and the VERTIGO (VERtical Transport In the Global Ocean) study have captured spatial variability greater than the previously observed seasonal variability (Buesseler et al., 2009). Although these observations strongly suggest that rapid biological and physical processes occurring at small spatial scales may be involved in the transfer of surface production to the deep ocean, their spatial resolution is still insufficient to quantify and explain the processes leading to such localised fluxes.

The difficulty of measuring particle flux at high spatial resolution using observational methods makes the use of a model particularly attractive for understanding the impact of small-scale dynamics on export. As previously mentioned, numerous modelling studies have investigated the role of small-scale dynamics on the transport of tracers (including nutrients and dissolved organic matter) and on primary production. Some models coupling ocean dynamics with biogeochemical modules have demonstrated enhanced subduction of phytoplankton due to small-scale dynamical structures (Lévy et al., 2001, Plattner et al., 2005, Lathuillière et al., 2010), which has also been observed in situ (Fielding et al., 2001; Allen et al. 2005). Martinez and Richards (2010) showed that the spatial heterogeneities induced by lateral stirring in the euphotic zone may impact the temporal and spatial distribution of the particle flux out of the mesopelagic zone. However, to date, no study has specifically investigated the impact of small-scale dynamics on particulate export with a dedicated 3-D biogeochemical model including the mid-water column.

In this study, an existing biogeochemical model in a simplified setting of the north Atlantic (Lévy et al. 2010) is used to explore how small-scale dynamics influence estimates of particle export. To constrain particle export, ^{234}Th, which is the measuring method that provides highest spatial resolution of export estimates at present, was introduced into this biogeochemical model. This paper is structured as follows. In section 2 the model setting is presented. In section 3 the basin-scale and seasonal variability in the model are evaluated against available observations. Section 4 investigates the small-scale spatial variability in particle export using observations of thorium activity and evaluates the model's ability to reproduce such variability. Section 5 uses the model to examine how accurately field studies using thorium-234 can estimate export, given limitations on the temporal and spatial sampling coverage that can be achieved during cruises. Specifically, the impact of physical transport on thorium-234-derived export estimates is assessed (a factor that is often disregarded in thorium-234 studies), as are the impacts of undersampling and of assuming that the thorium-

234 activity is in steady-state. Section 6 discusses the main results and gives a synthesis of the mechanisms impacting export estimates.

2. Model setting and evaluation

2.1 Model configuration

The setting is a double-gyre representing an idealized North Atlantic basin. The model geometry is a closed rectangular domain on the β-plane of dimension 3180 × 2120 × 4 km, centered at 30°N and rotated by 45° anti-clockwise. We used output from the physical model run described in Lévy et al (2010). In this run, the horizontal resolution was 1/54° (2km). There were 30 z-coordinate vertical layers, varying in thickness from 10 to 20 m in the upper 100 m and increasing up to 300 m at the bottom. The level-coordinate free-surface primitive equation ocean model NEMO (Madec, 2008) was used. The circulation was forced with seasonally varying zonal profiles of wind, solar radiation, heat and salt fluxes. The atmospheric forcing generates a strong jet (the model equivalent of the Gulf Stream), which runs diagonally across the domain, separating a warm subtropical gyre from a colder subpolar gyre (Fig. 1). The jet is baroclinically unstable, leading to strong mesoscale turbulence, particularly in the band around the jet.

Analysis of the spectral properties of the model's submesoscale turbulence reveals that the effective resolution of the model is of the order of 10 km i.e. 5 to 10 times larger than the numerical resolution (Lévy et al., 2012a). This means that scales below ~10 km are strongly dissipated in the physical model. A practical consequence is that tracer transport can be performed off-line on a grid degraded down to the effective resolution, which is of 10 km (more details are provided in Lévy et al., 2012a). Thus the solution obtained with the physical model at 1/54° was degraded down to 1/9° in order to run the biogeochemical model off-line (with a gain of 10^3 in the off-line computating time). This degradation preserves the strength of the submesoscale horizontal and vertical velocities produced by the original model. As shown by Lévy et al. (2012a) with an off-line passive tracer experiment, the biogeochemical model is only slightly sensitive to the physical solution degradation.

2.2 Biogeochemical and thorium model

The biogeochemical and thorium model equations and parameters are provided in the Appendix (Table A2 to A5). The LOBSTER biogeochemical model (Resplandy et al., 2009) was used to calculate the biogeochemical tracer evolution. LOBSTER originally solved the evolution of six biogeochemical variables: phytoplankton (P), zooplankton (Z), detritus (D), semi-labile dissolved organic material (DOM), nitrate (NO3) and ammonium (NH4) (Fig A1 in Appendix). To account more fully for the range of particle sinking velocities observed in the ocean (Trull et al., 2008), we added a size-fractionated particle model that distinguishes between small slowly sinking particles (D) and rapidly sinking large particle (DD). To allow comparison with observations we estimated chlorophyll (Chl) concentration from phytoplanktonic nitrogen concentration using a constant N:Chl ratio equal to 1.32 g of chlorophyll per mol of nitrogen, which corresponds to a chlorophyll to carbon mass ratio of 1:60 and a C:N Redfield ratio of 6.6.

The model explicitly calculates the primary production of phytoplankton (calculating the uptake of nitrate and ammonium by phytoplankton separately), grazing of phytoplankton by zooplankton, and a simplified remineralisation network, which involves excretion by zooplankton, dissolution of detritus, accumulation of semi-labile DOM with subsequent remineralisation into ammonium, and ultimately, nitrification of ammonium into nitrate. The large detritus added to the model allows us to represent the increase of sinking speed with depth (Berelson, 2002; Gehlen et al., 2005) and the aggregation-disaggregation processes, which are necessary for reproducing the observed increase in the relative abundance of large particles with depth and the presence of small particles at depth (Murnane et al., 1994; Buesseler et al., 2009). Aggregation and disaggregation formulations were taken from the PISCES biogeochemical model (Aumont et al. 2003). Their rates are taken to be proportional to a prescribed turbulence parameter (noted shear in Appendix) and to the concentrations of DOM and small and large detritus. This non-linear formulation takes into account differential settling and turbulence coagulation mechanisms. The (dis-)aggregation coefficients (ϕ) were calculated from a power law size spectrum particle model (Kriest, 2002). Sensitivity tests showed that simulated values of export are sensitive to the large particles sinking speed parameter. However, the spatio-temporal variability of export (relative to the mean export value) changed only by 3% when decreasing the large particles minimum sinking speed from 200 to 50 $m.d^{-1}$, which gives confidence in the results presented here that mainly discuss the small-scale spatial variability.

We coupled the biogeochemical model described above with a model of thorium-234 (^{234}Th) dynamics. ^{234}Th is a particle-reactive radioisotope produced naturally by the decay of ^{238}U. Its relatively short half-life (24.1 d) makes it suitable to study processes such as particle export occurring over time-scales of weeks (Bacon and Anderson, 1982, Cochran and Masque, 2003). The temporal evolution of the total ^{234}Th activity (ATh) in the water column results from the balance between the radioactive production from ^{238}U (λAU*)*, the radioactive decay of ^{234}Th (λATh*)*, the export of ^{234}Th adsorbed onto sinking particles (*E*) and the dynamical advective and diffusive transports (Dyn):

$$\frac{\partial ATh}{\partial t} = \lambda(AU - ATh) - E + \mathrm{Dyn} \qquad (1)$$

where AU and ATh are the activities of ^{238}U and ^{234}Th respectively and λ is the decay constant of ^{234}Th (λ = 0.02876 d^{-1}). Measurements of ^{234}Th:^{238}U activity ratios less than 1 are taken to indicate loss of ^{234}Th via sinking particles. The combination of the ^{234}Th:^{238}U disequilibrium in the water column with POC/^{234}Th ratios measured on particles (Buesseler et al., 1992) are extensively used to constrain the particulate organic carbon (POC) export (Buesseler et al., 2006, Morris et al. 2007, Lampitt et al, 2008, Buesseler et al., 2009).

To represent the processes affecting ^{234}Th concentration (equation 1), we implemented a five-box model of ^{234}Th cycling (Fig. A1 and tables A1 to A5 in Appendix). The radioactive decay of ^{238}U supports the pool of dissolved ^{234}Th (Th_w) that undergoes a reversible adsorption to become particulate ^{234}Th (Th_{part}). Th_w and Th_{part} are both lost by radioactive decay. Th_{part} is distributed between the four particulate pools in direct proportion to their concentration: Th_P and Th_Z are respectively associated with suspended phytoplankton and zooplankton, Th_D with slowly sinking detritus and Th_{DD} with rapidly sinking detritus. *In situ* measurements indicate that the adsorption rate of ^{234}Th onto particles depends on the particle concentration, whereas the desorption rate is thought to be invariant with particle concentration (Bacon and Anderson, 1982; Honeyman et al., 1988; Dunne et al., 1997). In the model, ^{234}Th adsorption is therefore calculated with a second order kinetic law (Clegg et al., 1991, 1993; Murnane et al., 1994) and desorption with a first order kinetic law (see Appendix). We assume here that the rate constants for ^{234}Th adsorption and desorption (k_1 and k_{-1} respectively) are identical for all four particulate pools (phytoplankton, zooplankton, small and large detritus). Hence the reactive surface area of particles and the variability in adsorption that could arise from organic matter composition is not accounted for. We used values of k_1 and k_{-1} (see Tables in

Appendix) previously estimated from observations and an inverse model of the northwest Atlantic Ocean (Murnane et al., 1994). The model sensitivity to desorption and adsorption rates has been tested within the range of published values (Clegg and Whitfield, 1993; Cochran et al., 1993; Murnane et al., 1994; Murnane et al., 1996). Whereas the thorium model is insensitive to the desorption rate, it is quite sensitive to the value chosen for the adsorption rate. However, this sensitivity to the adsorption rate affects the absolute simulated values but does not influence their relative spatio-temporal variability. For example, the mean annual thorium deficit integrated between the surface and the equilibrium depth changes from 15200 $dpm.m^{-2}$ to 45060 $dpm.m^{-2}$ when the adsorption rate is increased from 2.10^4 to 9.10^4 $m^3.Kg^{-1}yr^{-1}$ but its spatio-temporal variability (estimated by its standard deviation) relative to the annual mean value only changes by 1%.

2.3 Model experiment

The offline biogeochemical model was run on the 1/9° resolution grid over three climatological annual cycles. Some of our results are presented as depth-integrals between the surface and the equilibrium depth (hereafter noted Zeq), which we define as the depth where AU- ATh < 50 $dpm.m^{-3}$. Zeq is therefore variable in time (Fig 4 b) and space (Fig 7 c). In equation (1), *E* is the thorium flux across the equilibrium depth. Note that this study examines the impact of physical processes only and that other key processes, such as the impact of the ecosystem assemblage on the remineralisation and organic matter export, are not considered here.

3. Basin-scale, seasonal variations and model evaluation

We first present the basin-scale distribution and seasonal cycle of simulated dynamical and biogeochemical fields that are most relevant for particle and thorium cycling. The physical solution has been analyzed in more detail in Lévy et al. (2010). The seasonal cycle and the large to small-scale variability of the biological system were presented in Kremeur et al. (2009) and Lévy et al. (2012b) respectively. Note, however, that these studies did not simulate the large detritus compartment or the thorium cycling.

3.1 Biogeochemical basin-scale contrast and seasonal cycle

The model simulates a cyclonic subpolar gyre in the north and an anti-cyclonic subtropical gyre in the south that are separated by a jet (model equivalent of the Gulf Stream) that flows eastward (Fig 1 a). This double-gyre structure primarily arises from the large-scale wind-forced Ekman upwelling and downwelling, which is combined with a marked latitudinal change in seasonal insolation and mixed layer depth (MLD). The simulated annual mean distribution of sea surface temperature (SST) and surface chlorophyll (Chl) is strongly influenced by the gyre circulation (Fig 1 a and c). In the subpolar gyre, deep winter MLDs and shallow thermocline and nutricline maintain cold, nutrient-rich waters close to the surface and promote phytoplanktonic production. In contrast, shallow MLDs and deep thermocline and nutricline in the subtropical gyre explain the presence of warm and nutrient-poor surface waters associated with low chlorophyll concentrations. Our experiment is idealized in many ways, which makes a point-by-point direct comparison with observations difficult. Nevertheless, the SST and surface Chl simulated in the model are very similar to those observed by satellite imagery in the North Atlantic (Fig 1).

The annual mean basin-scale distribution is modulated by the seasonality of the mixed layer, which largely depends on the region considered. In order to understand those differences, we consider three regions with different productive regimes that can be identified from surface Chl concentrations in both the model and observations: a “subtropical province” in the oligotrophic subtropical gyre ([Chl]<0.15 mg.m^{-3}, contour on Fig 1 c, d); a “subpolar province” in the northern subpolar gyre ([Chl]>0.3 mg.m^{-3}, contour on Fig 1 c, d); a “transition region” of intermediate Chl concentration where the jet flows (0.15<[Chl]<0.3 mg.m^{-3}, contour on Fig 1 c, d). Note that a fourth region of eastern boundary upwelling can be identified in the southeast ([Chl]>0.15 mg.m^{-3}, contour on Fig 1 c, d). However the model geometry is too simple to represent the complexity of the boundary upwelling system; this region will therefore only be briefly discussed in this work. In the subtropical province, the MLD remains fairly shallow (<100 m) preventing the input of nutrients and phytoplankton growth in the euphotic layer (Fig 2 a). The total particle concentration (phytoplankton, zooplankton and detritus averaged over 0:120 m) is therefore low all year round. In the transition region and the subpolar province, deeper ML input nutrients into the euphotic layer (Fig 2 b and c). Phytoplankton abundance increases in winter as the mixed layer deepens and brings nutrients into the euphotic layer (Fig 2). The bloom first develops in the transition region in January-February (Fig 2 b). It then propagates in the subpolar province while intensifying and following the large-scale mixed layer restratification that reaches the highest

latitudes in April (Fig 2 c). In response to the northward propagation of ML restratification, the bloom peaks in March in the transition region and in April in the subpolar province. The total particle concentration reaches its maximum two weeks after the bloom, when zooplankton and detritus are the most abundant (Fig 2 c). The bloom is then followed by a six-month period of low phytoplankton and total particle concentration.

3.2 Thorium model evaluation

To evaluate the model's ability to represent thorium dynamics, we use observations of total ^{234}Th activity (ATh) gathered in the open-ocean regions of the North Atlantic (see Fig 2 d for stations positions) during the following cruises: North Atlantic Bloom Experiment 89 (Buesseler et al., 1992), North Atlantic Bloom 08 (Martin et al., 2011); RRS Discovery 306, RRS Discovery 296 and Poseidon 300 (Lampitt et al., 2008); AMT12-14 (Thomalla, 2007; Thomalla et al., 2006); RRS Discovery 321 (Sanders et al., 2010), RRS Discovery 341 (Le Moigne et al., in revision). All available data were sampled between March and September. To account for the seasonal evolution and the northward propagation of the bloom, model results and data are compared over two periods (spring – March to May and summer/autumn – June to September) and in the three regions defined previously from the annual mean Chl concentration in observations and the model (Fig 3, refer to Fig 2 c and d for definition of regions). The thorium model is evaluated using the deficit in total ^{234}Th activity (ATh deficit = AU-ATh), which primarily reflects the magnitude of ^{234}Th scavenging (E in Eq. 1). To first order, a large deficit in ATh indicates substantial export of ^{234}Th on sinking particles (Fig A1-model chart), whereas low deficit values are associated with low particle fluxes. Note that a deficit in ATh of ~2500 dpm.m^{-3} indicates complete depletion of ^{234}Th, as AU in the observations and the model ranges from 2450 to 2600 dpm.m^{-3}.

Although the physical and biogeochemical models are highly idealised, the model range of ATh deficit is reasonably comparable to the one observed (symbols on Fig 3). ATh deficit values are generally higher toward the surface, where particulate concentrations are large and decrease with depth as particles are degraded. Subsurface excesses in ATh (deficit<0) occur due to release of ^{234}Th into the dissolved phase when thorium-rich sinking particles are remineralised. At greater depths, where particle concentrations are low, AU and ATh are in equilibrium and the ATh deficit is close to zero. The exact shape of the ATh deficit profiles varies latitudinally and seasonally (Fig 3). ATh deficits in the particle-poor environment of the subtropical province are small (< 500 dpm.m^{-3}) from spring to autumn (Fig 3 e and f). In

the transition region, observed surface deficit values (~2000 dpm.m^{-3}) are highest in spring when the particle concentration peaks and decrease (< 1500 dpm.m^{-3}) in summer/autumn when the particle concentration drops (Fig 3 b and d). In contrast, observed ATh deficits in the subpolar province show an increase from spring to summer/autumn (Fig 3 a and b). The range of ATh deficit simulated in the model reproduces the main observed features (black lines on Fig 3). The sharp latitudinal contrast in ATh deficit between the oligotrophic subtropical province and the two productive regions is simulated. The model also indicates a seasonal decrease (increase) of ATh deficits in the transition region (subpolar province) between spring and summer/autumn. Another interesting feature captured by observations is the change in the shape of the ATh profiles between spring and summer/autumn in the two productive regions (Fig 3 a-d): subsurface gradients are sharpened and the depth of equilibrium between AU and ATh is shallowed by approximately 200-300 m. The model also simulates this change, which gives us confidence that it is to first order forced by a dynamical process and not associated with an internal shift in the ecosystem (plankton assemblage, particle size and composition etc.), since these factors are not included in the model. Between spring and summer the water column stratifies further. Deep spring mixed layers mix ATh vertically, whereas summer shallow mixed layers confine large ATh deficit values created at the surface to the upper water column.

However, some shortcomings of the model are noteworthy. The model fails at representing the range of values seen below 300 m in observations (Fig 3). This misfit cannot be explained by a decrease of spatial and temporal variability in physical processes at depth but more likely by the model simplicity in representing biogeochemical processes in the water column (two particle sizes, one remineralisation rate etc.). Also, ATh deficits simulated in the subtropical province are larger than in observations (Fig 3 e and f). It is possible that part of this bias is due to the undersampling of this region (Fig 1 d). However, it is very likely that the simplicity of the biogeochemical model also explains a large part of this misfit. Indeed, our biogeochemical model includes only one phytoplankton and one zooplankton (with one set of parameters for each), which limits the ability to reproduce in details the contrasted regimes (oligotrophic to productive) found in the domain.

In summary, the model's performance in capturing the phytoplankton (Chl) concentration and Th activity mean state is adequately realistic in the three different regions identified in the North Atlantic. The model simplicity most likely leads to an overestimation of ATh deficits in the subtropical province and to an underestimation of the range of ATh deficits below 300 m.

However, it is found that the model faithfully reproduces the contrast between the three regions and the seasonal changes captured by the observations. The simplicity of the model geometry and biogeochemistry is indeed mandatory to perform high-resolution simulations that reproduce the sub-mesoscale spatial variability.

4. Observed and simulated spatial variability at the (sub-)mesoscale

We illustrate the spatial variability at small-scale in the model with snapshots on the 18th of March (Fig 4). On this date the bloom and the particle export at the equilibrium depth peak at mid-latitudes but has not yet reached the northern part of the subpolar gyre where ML are deeper (Fig 4 a, c and d). The adsorption and export of ^{234}Th onto the particles associated with the bloom has lowered the surface ATh at mid-latitudes, whereas it is higher in the particle-poor regions of the subtropical gyre and the northern part of the subpolar gyre (Fig 4 b and d). Note that the spatial offset between the export and the ^{234}Th flux at the equilibrium depth is discussed in section 6. The basin-scale distribution of particles and ^{234}Th variables are all modulated by structures at the mesoscale and submesoscale (1-100 km) (Fig 4). Because eddies in the model are mostly generated through baroclinic instability of the main jet (30-35°N), the spatial distribution of eddies and filaments is highly heterogeneous (Lévy et al, 2010). Large eddies (100-200 km diameter) predominantly appear close to the western boundary, where the jet is most intense, and propagate into the two gyres. The emergence of the smaller eddies and the filamentary structures that significantly influence the phytoplankton concentration, the export and the thorium distribution across the domain result from the non-linear interactions between these large eddies (Fig 4).

To assess the model's ability at representing small-scale spatial variability, we compare the eddy kinetic energy (EKE) and the surface Chl spatial variability at small-scale in the model and in observations (Fig 5). To quantify the spatial variability of surface Chl, we calculate a diagnostic, denoted SV_{100km}, that quantifies the mesoscale spatial variability within a radius of 1° (~100 km). The SV_{100km} of X, calculated at each point *i* and time *t*, corresponds to the spatial standard deviation (noted std) of X within a 100x100 km box:

$$SV_{100km}(X_{i,t}) = \mathrm{std}(X_{i,t}, 100\ \mathrm{km}) \qquad (2)$$

where, at each point *i* and time *t*, ($X_{i,t}$, 100 km) is the set of variable values in a 100x100 km box centred on *i*. This measure can be interpreted as follows: if a region is homogeneous at

scales up to ~100 km, the SV_{100km} will be low; if the spatial variability is large at these scales the standard deviation, and consequently SV_{100km}, will be large.

Because eddies are mostly generated through baroclinic instability of the Gulf Stream, the observed spatial distribution of the EKE is highly heterogeneous (Fig 5 b). The region of highest EKE (> 0.15 $m^2.s^{-2}$) is located in the offshore extension of the jet. Areas of moderate EKE (> 0.05 $m^2.s^{-2}$) also develop on the southern and northern flanks of the jet in the subtropical and the subpolar gyres. The model reproduces the amplitude of EKE in the jet region and the subpolar gyre but overestimates the variability in the subtropical gyre (Fig 5 a). The small-scale spatial variability of SeaWiFS Chl (SV_{100km}, Fig 5 d) increases with Chl concentration (Fig 1 d). In both observations and the model, the annual mean SV_{100km} is lower than 0.05 $mg.m^{-3}$ in the subtropical province, lower than 0.1 $mg.m^{-3}$ in the transition region and reaches 0.3 $mg.m^{-3}$ in the subpolar province (Fig 5 c and d). Although mean Chl concentrations are relatively well represented (Fig 5 c and d), the model underestimates the Chl spatial variability in the eastern part of the transition region and in the southern part of the subpolar province (Fig 5 c and d).

Although SV_{100km} cannot be calculated from in-situ ATh due to the lack of observations, there is some data that shows variability at small-scale. The study of Buesseler et al. (2009) used an extensive ^{234}Th data set to explore the spatial (10-100 km) and temporal (days to weeks) variability of particle flux at two sites in the north Pacific; the oligotrophic Hawaii Ocean Time-series (HOT) and the mesotrophic HNLC K2 site part of the VERTIGO program. This study displays variability in the ^{234}Th flux of about 215 $dpm.m^{-2}.d^{-1}$ at HOT and 1540 $dpm.m^{-2}.d^{-1}$ at K2 (defined as the standard deviation of the data set) on spatial scales of the order of 200-300 km, which represents a variability of 35-40%. Since the variability shows no clear N/S or W/E gradient, it was interpreted as variability related to the mesoscale (see Fig 3 of Buesseler et al., 2009), though submesoscale variability may equally be involved. The study also demonstrated an intense temporal variability of thorium related to the bloom decay at the mesotrophic site K2, which led to considerably different ^{234}Th flux estimates when accounting for these temporal changes or not (i.e. using a non-steady state or a steady-state approach, Fig 2 of Buesseler et al., 2009). One could argue that this large temporal variability and the asynopticity of the data sets, which were sampled over periods of ~20 days, may have biased the estimation of the spatial variability.

Here we present a quasi-synoptic data set sampled in the north Atlantic that further supports the existence of such spatial variability in ^{234}Th. As part of a NERC-funded UK research cruise on RRS Discovery (D341), ^{234}Th activity at 25 m, 50 m and 100 m depth was measured at high resolution with 10 stations located 25 km apart and within a 100 km radius around the productive PAP site (49.5°N, 16.5W). This data set is considered to be synoptic because the 10 stations were sampled in less than 72 hours (3rd August 2009, 17:00 – 6th August 2009, 06:00). See Table A1 in appendix and Le Moigne et al. (in review) for details on the data set. The spatial variability at small-scale estimated from this dataset ranges from 270 to 550 dpm.m^{-3} (435 dpm.m^{-3} at 25 m; 550 dpm.m^{-3} at 50 m and 270 dpm.m^{-3} at 100 m), which corresponds to a variability of the order of 25-50%. This estimate is very similar to the results of Buesseler et al. (2009), although the three sites considered (PAP, HOT and K2) contrast strongly in terms of latitude, seasonal cycle, ocean physics and ecosystem assemblage. Also note that Buesseler et al. (2009) calculated the spatial variability of the thorium flux, whereas the observations presented here are thorium activities. Indeed, to achieve such a high horizontal resolution sampling in a synoptic manner thorium activity was sampled at a low vertical resolution (three depths), from which the thorium flux cannot be inferred.

To explore the source of this small-scale spatial variability in thorium activity at PAP, the backward trajectories of the water parcels, located at each of the 10 stations where thorium was sampled, were computed from altimetric surface velocities (Fig 6, see Resplandy et al. (2009) for details on the method of backward trajectories calculation). Backward trajectories were calculated over 25 days because this is the maximal response time of thorium (~ ^{234}Th half life). The sampling site is located in a region of large strain resulting from the interaction of five large eddies (A1, A2 and C1 to C3 in Fig 1). Although the 10 stations are located within a 100 km radius, two clusters can be identified from their trajectories: one with a northwest-southeast trajectory between eddies A1 and C2, characterised by rather high thorium activities (in blue); one with a circular trajectory that followed the southern flank of eddy C2 and then the northern flank of eddy C3 (in red), characterised by lower thorium activities (in red). The interaction between the eddies generates filaments, stirring together the two water masses, placing side by side waters with biogeochemical characteristics of a larger scale gradient. This suggests that the spatial variability captured by the ^{234}Th dataset is derived from the patchiness in particle export arising from the stirring of gradients from the large-scale to the small-scale by mesoscale oceanic structures. Furthermore, this dataset provides evidence that the degree of horizontal spatial variability varies vertically (40% at 25

m; 50% at 50 m and 25% at 100 m), though, as only three depths were sampled, no trend can be inferred.

The spatial variability of thorium in the model is explored by analysing the spatial patterns of the SV_{100km} (Fig 7). SV_{100km} is calculated on a specific date during the bloom (on March 18th, Fig 7 a and b), which allows a comparison of the simulated spatial variability with the estimates from observations and over an annual mean (Fig 7 c and d), which smoothes out specific structures and provides an integrated view of the patterns. During the bloom, the simulated SV_{100km} for the Th flux roughly ranges from 0 to 1000 dpm.m^{-2}.d^{-1} with values larger than 1000 dpm.m^{-2}.d^{-1} in the northern part of the domain (Fig 7 b). The spatial variability on scales of 100 km is about 100-300 dpm.m^{-2}.d^{-1} in the oligotrophic region and about 200-1000 dpm.m^{-2}.d^{-1} in the more productive regions, which is comparable with the estimates derived from observations in the North Pacific (~215-1540 dpm.m^{-2}.d^{-1} on spatial scales of 200-300 km in Buesseler et al., 2009). The SV_{100km} for surface ATh deficit in the model ranges from 30 to 300 dpm.m^{-3} (Fig 7 a). In the region where the PAP site is located (north of the subpolar province), the spatial variability is of the order of 100-200 dpm.m^{-3} on spatial scales of 100 km, which although it is comparable is significantly lower than the spatial variability found in observations (270-550 dpm.m^{-3}).

For the annual mean, surface ATh and thorium flux at Zeq present similar SV_{100km} patterns (Fig 7 c and d). The small-scale spatial variability of thorium fields (Fig 7) is primarily explained by the patterns of eddy kinetic energy (Fig 5 a). Highest values of SV_{100km} are located in the highly energetic region of the jet. Moreover, the patterns in SV_{100km} for thorium fields reflect the contrast between the oligotrophic subtropical province, where the surface Chl SV_{100km} is low and the productive subpolar province where the Chl SV_{100km} is higher (Fig 7 c). The model also simulates a region of high small-scale variability along the southeastern border where the upwelling occurs (Fig 7). In this region, the EKE is not particularly intense but large horizontal gradients are created by sub-mesoscale filaments emanating from the productive upwelling and extending into the low productivity subtropical gyre (Fig 4 a).

The model ability at representing the mean state but also the spatial variability at small-scale has been evaluated using both satellite (EKE, Chl) and in-situ observations (ATh deficit and Th flux). Although the model is highly idealised in terms of geometry, atmospheric forcing and biogeochemistry, it reproduces most of the features characteristics of the three different

biogeochemical provinces. Hence we expect that the model is suitable to examine the influence of (sub-)mesoscale physics on ^{234}Th and on the export estimates derived from it.

5. Impact of small-scale dynamics on ^{234}Th flux estimates

The model demonstrates strong spatial variability in physical (Fig 5 a), biological and thorium dynamics at scales less than 100 km (Fig 4, Fig 5 and Fig 7). Does this variability affect the robustness of export estimates made using conventional field methods? To tackle this question, we focus on export obtained from *in-situ* thorium measurements because it is at present the proxy used to estimate export at small spatial and temporal scales. Standard assumptions made when estimating export from thorium include steady-state and minor contribution from ocean dynamics. In this section we use the model to quantify the contribution of ocean physics to the thorium budget and to estimate the errors associated with spatial and temporal undersampling. We then test the impact of assuming that thorium activity is in steady-state and of sampling in a Eulerian manner at a fixed location over time.

5.1 Contribution of physical processes to the thorium budget

From equation (1), the thorium flux (*E*) across the equilibrium depth (*Zeq*) can be expressed as:

$$E_{z=Zeq} = \int_{z=Zeq}^{0} (\lambda(AU - ATh) - \frac{\partial ATh}{\partial t} + \mathrm{Dyn}).\ \mathrm{dz} \qquad (2)$$

The dynamical transport (Dyn) includes horizontal and vertical advection and diffusion. The vertical turbulent diffusion term is mostly accounted for by mixing. In contrast, the horizontal turbulent diffusion of ATh is assumed to parameterise the horizontal transport by small-scale transport due to sub-grid processes, which by definition are not resolved by the model. It is therefore included in the horizontal advective term here. The total physical transport of ATh (*Total*) and the contributions of horizontal advection (Ha), vertical advection (Za) and mixing (Mix) are integrated between the surface and the equilibrium depth (Zeq):

$$Ha = \left(\int_{z=Zeq}^{0} (\underbrace{-u_H \nabla_H ATh}_{\text{horizontal advection}} + \underbrace{\partial K_h \partial ATh / \partial h^2}_{\text{horizontal turb. diffusion}}).\mathrm{dz} \right) ;$$

$$Za = \left(\int_{z=Zeq}^{0} (\underbrace{-u_z \nabla_z ATh}_{\text{vertical advection}}).\mathrm{dz} \right)$$

$$Mix = \left(\int_{z=Zeq}^{0} (\underbrace{\partial K_z \partial ATh / \partial z^2}_{\text{vertical turbulent diffusion}}).\mathrm{dz} \right) \qquad \text{and} \qquad Total = Ha + Za + Mix$$

with *K* the turbulent diffusion coefficient and *u* the velocity in horizontal (H) and vertical (Z) directions. Fig 8 a shows the annual 95% confidence interval of the dynamical contributions. Note that a 95% confidence interval of 200 dpm. $m^{-2}.d^{-1}$ means that 95 % of the time (i.e. 95*365/100 ≈ 346 days a year), the dynamical transport contribution to the thorium flux is ≤200 $dpm.m^{-2}.d^{-1}$. Note that Mix is found to be one order of magnitude lower than Ha and Za and is not presented in Fig 8.

Physical transport contributes to the thorium budget mainly in the jet region where it modulates the thorium activity by 120 to 600 dpm. $m^{-2}.d^{-1}$. Outside the jet region, the physical transport of ATh is weaker, ranging from 60 to 180 dpm. $m^{-2}.d^{-1}$ in the subtropical gyre and the northern flank of the subpolar gyre and being lower than 60 $dpm.m^{-3}$ in the centre of the subpolar gyre (Fig 8 a). This correlates with the EKE pattern, clearly indicating that physical transport significantly impacts the thorium budget in regions populated with energetic (sub-)mesoscale structures (Fig 5 a and Fig 8 a). The contribution of horizontal advection is relatively low (≤120 dpm. $m^{-2}.d^{-1}$, Fig 8 b) and the major contribution is by vertical advection of thorium across the equilibrium depth (Fig 8 c). The importance of vertical advection in the region of high EKE is consistent with the results of Lévy et al. (2012b) which show that this region has high vertical velocities. Note that the vertical advection of ATh across the equilibrium depth is low in the upwelling region (south-east boundary, Fig 10c). In this region, vertical advection brings subsurface waters with low deficit in ATh close to the surface and therefore shallows the equilibrium. Vertical velocities (u_z) generally decrease toward the surface ($u_{z(z=0)}=0$), which explains the low values of the vertical advection across the shallow equilibrium depth.

5.2 Impact of undersampling

Strong horizontal gradients and variability at small spatial scales can bias regional estimates derived from in situ measurements that undersample the spatial variability (Resplandy et al., 2009). Here we quantify the impact of undersampling by comparing the regional (5°x5°≈

550x550 km box) thorium flux predicted by the model (noted E_{model}) to an estimate derived from sub-sampling of this region (noted E_{sample}). The size of the regions (5°x5° boxes) is relevant to an area that may include several mesoscale structures but still be amenable to sampling during a cruise. For each box, the model is sampled randomly by a "cruise", with a number of stations ranging from 2 to 50 stations. To obtain a statistical result, the random sampling or "cruises" are repeated 2000 times (using more was found to give the same result) in each box and at each sampling density. For each box, the undersampling error is given by the 95% confidence interval obtained for the 2000 estimates of $E_{sample} - E_{model}$. An error of 200 $dpm.m^{-2}.d^{-1}$ means that 95% of the "cruises" (i.e. 1900 over 2000) gave an estimate of the thorium (E_{sample}) flux within 200 $dpm.m^{-2}.d^{-1}$ of the model regional value (E_{model}).

The undersampling error is of course linked to the amount of spatial variability, regardless of sampling resolution (Fig 9 a, Fig 9 b and Fig 7 d). For the annual mean, the error is maximal in regions of highest SV_{100km}: the jet region where EKE is the highest and the northern subpolar gyre and upwelling region where productivity is more intense. The error decreases toward the interior of the gyres. While this pattern is independent of sampling density (Fig 9 a and Fig 9 b), the error increases as the sampling density decreases. The sensitivity of this model-derived error to the sampling density, to the season when the sampling is performed and to the asynopticity of the sampling is shown for boxes A (jet region) and B (subpolar gyre interior) on Fig 9 c. If the sampling is dense enough (25-100 stations), the flux is estimated with an error smaller than 400 $dpm.m^{-2}.d^{-1}$ regardless of the region (black crosses vs. diamonds) and the season (solid vs. dashed black lines). The estimated error however drastically increases when the coverage is scarcer (2-10 stations) and when the flux increases at the time of the bloom (dashed lines), in particular in regions of high spatial variability (Fig 9 c). It should be kept in mind though that while an absolute error of 400 $dpm.m^{-2}.d^{-1}$ represents a small error relative to the total flux in regions of high export (north of subpolar gyre), it represents a much larger relative error in regions of low export (subtropical gyre).

It is, however, crucial to consider the time needed to sample 10, 25 or 100 stations, as the asynopticity of a cruise may introduce a bias due to temporal changes in ATh. If the cruise takes place at a season of high temporal variability, the difference in ATh between stations sampled early and sampled late is likely to reflect the temporal evolution of ATh as well as the small-scale spatial variability. To estimate the impact of asynopticity, we applied the same method of sub-sampling in 5°x5° regions taking into account cruise durations of 30 and 50 days (Fig 9 c). Note that results obtained with cruise durations between 1 and 30 days are not

presented, as they do not differ significantly from the synoptic case. The asynopticity has a very weak impact on the error (minimal and maximum values) if the cruise duration does not exceed ~30 days (which corresponds to the integration time-scale of ^{234}Th, blue lines on Fig 9 c). In contrast, the maximal error is increased by about 400-600 dpm.m^{-2}.d^{-1} if the cruise lasts longer than ~30 days (green lines on Fig 9 c). However, taking 25 to 100 ^{234}Th profiles within 30 days implies a large sampling effort of 1 to 4 ATh profiles per day.

5.3 Models for calculating ^{234}Th flux

ATh *in situ* data are generally used to estimate the thorium flux (*E*) by solving equation (1) after simplifying assumptions. Physical transport is usually neglected by invoking minimal advection and diffusion of ATh relative to the downward flux of particulate thorium (Dyn=0). In most studies, Equation (1) is further simplified by assuming steady state conditions ($\partial ATh / \partial t = 0$). Using the steady state approach (noted SS), the net thorium flux across Zeq is thus proportional to the ATh deficit integrated over that depth:

$$E_{z=Zeq}(\mathrm{SS}) = \int_{z=Zeq}^{0} \lambda(AU - ATh).\,\mathrm{dz} \qquad (3)$$

Solving equation (1) while accounting for non-steady state conditions ($\partial ATh / \partial t \neq 0$ and $\mathrm{Dyn} = 0$) requires the study area to be reoccupied over time (t_1 and t_2). Using a non-steady state approach (noted NSS), the thorium flux is most commonly estimated from the linear interpolation of ATh between t_1 and t_2 ($\Delta t = t_2 - t_1$) as follows (Buesseler et al., 1992):

$$E_{z=Zeq}(\mathrm{NSS}) = \int_{z=Zeq}^{0} \lambda \left[\frac{AU(1-e^{-\lambda\Delta t}) + ATh_{(t_1)}e^{-\lambda\Delta t} - ATh_{(t_2)}}{1-e^{-\lambda\Delta t}} \right].\,\mathrm{dz} \qquad (4)$$

By comparing the thorium flux predicted by the model (equation (2)) to the estimates using the steady state and non-steady state approaches at each point of the model (equations (3) and (4) respectively), we estimate the error associated with these widely used approximations. An error of 1000 dpm.m^{-2}.d^{-1} means that 95% of the time the method gives an estimation of the thorium flux within 1000 dpm.m^{-2}.d^{-1} of the truth. As for the errors estimated in the case of undersampling (section 5.2), the model estimated errors presented here thus represent the worse case scenario in the model. This means that the difference between the estimated thorium flux and the calculated thorium flux will generally be lower or equal to the model-derived error in particular in regions and periods of low export flux.

The SS method approximates the thorium flux within 600 to 1000 dpm.m^{-2}.d^{-1} of the true value in the subtropical gyre and the jet region and within 1000 to 2000 dpm.m^{-2}.d^{-1} in the subpolar region (Fig 10 a). When considering the error relative to the Th flux, the north-south contrast is smoothed out and the predicted error is of the order of 40-60% over most of the domain. However, in the northern subpolar gyre and the upwelling regions that are regions of intense blooming and export where ^{234}Th flux shows strong temporal variation, the estimated errors reach values larger than 2000 dpm.m^{-2}.d^{-1} (i.e. 60-80% of the Th flux).

The NSS approximation is compared to the model Th flux considering two different sampling intervals ($\Delta t=t_2-t_1$= 10 days and 20 days). In both cases, the NSS approach always gives errors larger or equal to that using the SS. For both time intervals the error is largest in the jet region, the subtropical gyre and the upwelling (Fig 10 b and Fig 10 c). The error decreases from the 10-day to the 20-day sampling interval. In the subpolar gyre, the 20-day NSS thus approximates the thorium flux with an error similar to the SS approach (600-1000 dpm.m^{-2}.d^{-1} i.e. ~40-80%) whereas the 10-day NSS gives a poorer estimate (> 1000 dpm.m^{-2}.d^{-1} i.e. ~50-150%). Although the estimated errors are still large, the most striking improvement between the 10-day and 20-day NSS occurs in the regions of high spatial variability, where errors drop from values larger than 2000 dpm.m^{-2}.d^{-1} to values lower than 2000 dpm.m^{-2}.d^{-1}; these are also regions where both NSS estimates do not represent the model flux as well as the SS estimate. In these regions of high spatial variability, the change in ATh between t_1 and t_2 is more representative of the small-scale spatial gradients than of the seasonal signal. By increasing Δt the impact of small-scale structures is reduced, and the NSS estimate is improved.

A way of limiting the impact of small-scale spatial variability in the NSS approach is to perform Lagrangian sampling, optimally in a coherent structure such as an eddy. To test this hypothesis, we compared the model thorium flux with the estimates using SS and NSS approximations within three eddies located in those regions where the Eulerian NSS approach resulted in particularly large errors. To reproduce Lagrangian methods used *in situ* (Martin et al, 2011; Smetacek and Naqvi, 2008), we identified contrasting eddies in the model using SST and sea-surface phytoplankton concentrations (Fig 1). The thorium flux simulated at a fixed station located at the eddy E1 starting point decreases from March to May because the “large-scale” bloom at this latitude has already occurred (grey line on Fig 11 a). In contrast, the thorium flux predicted along the track of E1 increases in March in response to the development of phytoplankton inside the eddy (not shown) and then decreases with

phytoplankton and particle concentrations in April (black line on Fig 11 a). The first notable result is that the thorium flux at a fixed station (starting point of eddies) shows greater variations at high frequency (<10 days) than the thorium flux at the centre of E1 (Fig 11 a). Second, the comparison of the thorium flux estimated with a NSS method at the fixed station (eddy starting point) with the flux predicted by the model at this same station shows errors larger than 50% (grey bars on Fig 11 b) and which can reach values above 100% when the thorium flux varies rapidly (for example in early April on Fig 11 a). These two results support our previous finding that the variability sampled at a fixed station is more representative of small-scale spatial gradients than of the seasonal signal and explain the relatively poor results of the NSS approximation in a Eulerian context.

In comparison, the thorium flux calculated with a Lagrangian NSS approach estimates the thorium flux predicted by the model along the track of E1 with errors lower than 25%. As expected, in this Lagrangian framework the flux estimation is improved when using the NSS method instead of the SS approach. However, this result cannot be generalised. Indeed, in eddy E2, the Lagrangian SS and NSS approaches both give estimates with errors of the order of 25-50%, which is comparable to the Eulerian NSS estimates computed at the fixed station (Fig 11b). This substantial difference in the quality of the Lagrangian NSS estimate can be explained by the amplitude of the dynamical transport of thorium along the eddy track (Fig 11 c). Whereas the dynamical contribution to the thorium budget at the centre of E1 is very low, it is quite large at the centre of E2 (Fig 11 c). This comparison between two eddies illustrates that not all eddies are coherent structures fully isolated from the surrounding waters and that they do not necessarily provide a “true” Lagrangian framework.

6. Discussion

6.1 Spatio-temporal decoupling between phytoplankton, export and thorium

In the model, the spatial variability of particle export and phytoplankton are very similar at small-scales (Fig 4). Observational studies indicate that the variance for phytoplankton abundance can be contained at larger (Tsuda et al., 1993) or smaller (Martin and Srokosz, 2002) spatial scales than that for zooplankton (see Martin 2003 for a review), and this uncertainty is much larger for the relationship with export. Nevertheless, the model results are consistent with theoretical work on reactive tracers (Neufeld et al., 1999; Hernández-Garcia et

al., 2002; Tzella and Haynes, 2007). As highlighted by Martin and Srokosz (2002), the interactions governing the ecosystem (grazing time lag for example – see Tzella and Haynes, 2007) and the use of one zooplankton size-class is unlikely to represent the variety of biological behaviour observed *in-situ*. Buesseler et al. (2009) suggested that this decoupling between phytoplankton and zooplankton could explain the observed lack of correlation between phytoplankton related fields (pigments, production) and particle export estimated from thorium. In our model, the patchiness in thorium activity and flux is indeed slightly different from the one of phytoplankton (Fig 4). However, this is not related to decoupling between phytoplankton and particle export, which show very similar variability in the model. The difference is instead caused by the integration time-scale of ^{234}Th. The spatial distributions of variables such as phytoplankton and particle export reflect the instantaneous dynamical transport (currents, eddies etc.), slightly smoothed out by processes with time-scales of a few days (primary production, export of large sinking particles). The thorium integration time scale is a function of both its half-life and removal time scale (Turnewitsch and Springer, 2001). In the model, the removal time scale of thorium is strongly related to the export of large sinking particles and can not explain the differences between ^{234}Th and particles distribution. The thorium distribution is in contrast smoothed out further because radioactive production and decay of ^{234}Th operate on longer time-scales, given its ~24-day half-life. We verified this hypothesis by running an additional simulation of the same model, but imposing a thorium half-life of 2 days. In this simulation, the spatial variability of surface thorium activity and thorium flux was identical to the variability of phytoplankton and particle export, confirming that the difference in spatial variability was due to the longer integration time-scale of thorium.

This difference in the integration time-scales also explains the spatial and temporal offset between the maxima in particulate export and in thorium flux (Fig 4). At the time of the bloom peak (March 18th), particle and thorium export are both highest in the northern part of the domain (Fig 4 c and Fig 4 d). However, the locations of maximum values in thorium flux are shifted northward from that of maxima in particulate export. This spatial shift results from the northward propagation of the bloom and the different time scales at which thorium and the bloom equilibrate with the ocean physics. As the bloom propagates northward, thorium is quickly depleted at each latitude, while particle export only peaks a few weeks later. Thorium is restored on the timescale of decay, which is much longer than that associated with the bloom. This spatial and temporal decoupling between phytoplankton-related fields and

thorium export in the real ocean could be enhanced or compensated by biogeochemical processes not represented in the model, such as the variety of biological interactions governing phytoplankton and zooplankton distributions at small-scale (Martin and Srokosz, 2002).

6.2 Small-scale dynamics and thorium flux

Thorium activity and thorium flux in the model are strongly variable on spatial scales of eddies (mesoscale) and smaller (sub-mesoscale). The strength of this small-scale variability (100-300 dpm.m^{-3} and 100-1000 dpm. m^{-2}. d^{-1} over 100 km for Th activity and flux respectively) exhibited by the model is supported by the few *in-situ* measurements taken at a resolution that can capture the patchiness of thorium activity at these scales (see section 4 and Fig 6).

This study confirms that the thorium flux at the equilibrium depth in the open ocean is quite insensitive to the horizontal transport of thorium, which accounts for less than 120 dpm. m^{-2}.d^{-1} i.e. a contribution lower than 15% of the thorium flux (Fig 8 b). In previous works, the impact of horizontal transport was considered in upwelling and coastal environments where large-scale ^{234}Th activity gradients are large. In the Equatorial Pacific, the influence of horizontal diffusion of recently upwelled deep ^{234}Th-enriched waters on the thorium flux was estimated to ~30% (Dunne and Murray, 1999). In the Gulf of Maine, the role of horizontal advection-diffusion of alongshore ^{234}Th-poor waters (originating from the more productive coastal area) and of offshore ^{234}Th-rich waters on thorium flux was evaluated between 30 and 100% (Gustafsson, et al. 1998; Benitez-Nelson et al., 2000, Charette et al., 2001). Although the estimates of horizontal transport in these regions are comparable, the relative contribution of horizontal diffusion and advection are a matter of debate. Whereas most studies found a dominant impact of horizontal diffusion (Gustafsson, et al. 1998; Dunne and Murray, 1999; Benitez-Nelson et al., 2000), advection was found larger than diffusion in Charette et al. (2001). This discrepancy is mainly related to the different horizontal resolution considered in those studies. Indeed, horizontal turbulent diffusion estimated from model and/or data parameterise the transport due to small-scale processes that are not resolved by the model or the data (sub-grid processes). While horizontal transport by small-scale processes (10-100 km) is parameterised by horizontal turbulent diffusion in low horizontal resolution studies, it is accounted for by advection in studies resolving those small scales, such as the one of

Charette et al. (2001) and the present study. In the latter case, strong small-scale gradients are mostly caused by the filamentation process also known as the tracer direct cascade (Abraham et al., 2000, Lévy and Klein, 2004). Eddies, and submesoscale filaments generated by the interactions between these eddies, are delimited by dynamic barriers that allow the transport of water masses while limiting mixing with the surrounding waters. Consequently, small-scale features in thorium activity mainly result from the horizontal cascade, stirring together waters with different rates of particle production and export without dissipating them. The relatively short time scale of the bloom and thorium cycling (about a month) explains the apparent discrepancy between this result and the traditional view that small-scale physics tends to homogenise thorium distribution.

The influence of horizontal transport derived from our model is also in the lower range of previous estimates performed for oligotrophic and productive regions of the open ocean. Savoye et al. (2006) gave a rough estimate of the impact of horizontal transport combining thorium export fluxes found in oligotrophic (500-1000 $dpm.m^{-2}.d^{-1}$) and productive (>3000 $dpm.m^{-2}.d^{-1}$) regions with current speeds typical of low energy (1 $cm.s^{-1}$) and high-energy (10 $cm.s^{-1}$) ocean physics and assuming small-scale changes of the order of 100-300 $dpm.m^{-2}.d^{-1}$. They found an impact of horizontal transport of the order of 15% in oligotrophic areas and of 20-50% in more productive areas, which is much larger than the result of the present study. The discrepancy between their estimate and our model results does not arise from differences in the magnitude of small-scale gradients or ocean current velocities. Rather, as described above, horizontal advection creates strong small-scale gradients by spatially redistributing different water masses within structures (eddies and filaments) that are delimited by transport barriers (d'Ovidio et al., 2010). This Lagrangian redistribution transports all properties (particles, thorium etc.) of a given water mass equally, while limiting the exchange with other water masses – and thus does not affect the thorium budget in any given water mass appreciably. Note, however, that the horizontal spatial variability assessed in this study could be underestimated: the spatial resolution is insufficient to assess the amplitude of the variability at scales of 10 km or smaller and the model is likely to underestimate the spatial variability in thorium activity (as well as chlorophyll) in the subpolar region.

In contrast, our model suggests that vertical advection can change the total thorium activity between the surface and the equilibrium depth by 100-600 $dpm.m^{-2}.d^{-1}$ (Fig 8 c). This is due to the sharp vertical gradients of thorium created by downward particle fluxes; vertical movement of water across the equilibrium depth therefore allows exchange between surface

waters low in thorium and subsurface waters high in thorium. The impact of vertical advection on the thorium budget is most important in regions of high eddy kinetic energy where it represents a change of 30-50% in the thorium export flux (Fig 5 a and Fig 8 c). In these regions of high kinetic energy, large vertical velocities are associated with the process of frontogenesis. Eddies and filaments are delimited by density fronts that become unstable as the eddy field is deformed. The re-stabilisation of these fronts, through frontogenesis, is associated with an ageostrophic circulation promoting vertical velocities on either side of the front (Klein et al. 1998). In contrast, the impact of vertical advection in the oligotrophic and subpolar gyres is much reduced and changes the thorium flux by less than 20% (Fig 8 a). In previous work, the role of vertical advection has mostly been considered in upwelling environments. Its impact was estimated to be ~50% in the Equatorial Pacific open-ocean upwelling (Buesseler et al., 1995; Bacon et al., 1996) and the Arabian Sea coastal upwelling (Buesseler et al., 1998). It is interesting to note that, although the influence of vertical advection induced by small-scale structures is weaker in most regions, its magnitude in high-energetic regions is comparable to the one observed in large-scale upwelling settings. More recently, Maiti et al. (2008) estimated the impact of Ekman pumping vertical advection on thorium flux estimates along the trajectory of an eddy. They found that ^{234}Th export fluxes increased by as much as five-fold (200 to 1500 dpm.m^{-2}.d^{-1}) depending on the upwelling velocity (1 to 3 m.d^{-1}). Although vertical velocities in our model are of the same order of magnitude or larger (1-3 m.d^{-1} at the gyres center and 3-10 m.d^{-1} in the jet region and northern subpolar gyre, see Fig 6 a of Lévy et al., 2012b), the impact on thorium flux estimated in the model using a eulerian method (Fig 8 c) and at the centre of two eddies using a lagrangian method (Fig 11 c) in is in the lower range of the estimation by Maiti et al. (2008). This can be explained by the different physical processes considered in both studies. Maiti et al. (2008) assumed a constant positive Ekman pumping at the center of an eddy, which results in a significant increase in thorium activity in the upper water column. In contrast, although Ekman pumping is present in our model, its intensity is lower than vertical advection associated with small-scale fronts around eddies (see mechanism of frontogenesis above). As these vertical movements are of different sign on either side of the small-scale fronts, their impact on thorium activity is lower. The relative importance of Ekman pumping in eddies and vertical advection associated with smaller-scale fronts is still a matter of debate and clearly requires further research (see Lévy et al., in revision, for a review).

Our study shows that the impact of the deepening of the mixed layer on the thorium budget is very low. This is because the reference depth at which the flux is calculated is based on the deficit in thorium activity (the equilibrium depth, where AU-ATh ≤ 50), which varies in time and space similarly to the mixed layer depth. For mixing to introduce disequilibrium in the thorium budget two conditions are required: 1) the mixed layer must be shallower than the equilibrium depth before the mixing event and deeper afterwards; 2) the presence of a vertical gradient of thorium created by prior particle export events. However, even if these conditions are fulfilled, when the mixed layer deepens, high thorium activity waters from the subsurface are mixed with surface waters of lower activity and the equilibrium depth is therefore deepened. This correlation between the evolution of the mixed layer depth and the thorium equilibrium depth explains why mixing has such low impact. When in situ measurements of thorium are used to estimate particle export, the contribution of physical transport is usually neglected. Our study indicates that this hypothesis is valid in regions of low eddy kinetic energy (Fig 8 a). Typically, the contribution of physical transport to the thorium budget is lower than 15% in regions where the annual mean eddy kinetic energy is lower than 0.15 $m^2.s^{-2}$. In regions of higher eddy kinetic energy, neglecting the contribution of ocean dynamics, and in particular of vertical advection associated with mesoscale and smaller structures, could introduce errors in the estimated thorium flux of 20-50%. If we generalise this result using the eddy kinetic energy derived from altimetry, it appears that the regions where the contribution of the ocean dynamics may have a significant impact on the thorium budget are mostly associated with western boundary currents and the Antarctic Circumpolar Current (Fig 9), regions of considerable primary production.

6.3 *In situ* observations and error introduced by spatial variability

In addition to the uncertainty associated with the dynamical transport of thorium, the presence of small-scale spatial variability can further bias the thorium flux derived from observations in two further ways. First, observed profiles of thorium activity essentially sub-sample the spatial variability at the mesoscale and smaller. While such observations give useful information on the order of magnitude and large-scale gradients of export (contrast between the sub-tropical and sub-polar gyres for example), the sub-sampling of thorium variability makes the estimation of the mean regional export difficult. The flux estimated by sub-sampling model outputs at low resolution departs from the true simulated flux by 400-1000

$dpm.m^{-2}.d^{-1}$. Our model suggests that this bias is greatly reduced, to values lower than 200 $dpm.m^{-2}.d^{-1}$, by increasing the sampling density from 2 to 25 stations for a 5°x5° region (i.e. sampling resolution of the order of 100 km). Increasing the number of stations implies longer sampling periods and increases the asynopticity of the data set. In our model setting, errors associated with asynopticity are, however, much smaller than the one introduced by spatial undersampling, in particular if the sampling period is shorter than ~30 days.

A second source of bias can be introduced when the non-steady state approximation is used (equation 4). Changes in thorium activity sampled at a station re-occupied over time (commonly two profiles taken 5 to 20 days apart) are typically interpreted as temporal changes. In agreement with the results of Savoye et al. (2006), we find that the uncertainty on the flux is higher over shorter periods between re-occupation (error larger with a 10-day period than with a 20-day period). Similar to their results, obtained with a compilation of data (data from 12 articles published between 1992 and 2005), we find that the difference between the non-steady state and the steady state approaches is reduced when the time delay between station re-occupation increases (because when Δt becomes large, $e^{-\lambda \Delta t}$ tends toward 0 and the non-steady state approach (equation 4) tend to the steady-state approach (equation 3) - refer to Savoye et al., 2006). A less expected result is that the errors associated with the non-steady state approach in our model (Fig 10 c) are generally higher than those obtained with the simpler steady state approach (Fig 10 a). This suggests that changes often interpreted as a temporal evolution are in fact due to patchiness in thorium activity at scales of the order of 100 km or below. This means that if the period before re-occupation increases from smaller to larger than the typical time needed to advect small-scale spatial structures past a point (typically 1-2 weeks in the model), the two samples are more likely to capture temporal changes of the mean spatial field rather than those associated with local spatial gradients. In contrast, the steady-state approach is unaffected by such spatial ‘contamination’. This result puts into perspective the prior assumption that the non-steady state approach is more accurate than the steady state approach in regions where the thorium activity varies temporally (such as blooming regions). Our study suggests that the non-steady state assumption is more accurate than the steady state assumption only if the contribution of temporal variability to the change between the two samples is larger than that of spatial variability. For example, our model predicts an improvement of the flux estimates when usisng NSS in regions of intense bloom and low eddy kinetic energy (northeastern flank of the subpolar gyre, Fig 10 a and c). The flux estimates is also improved when the sampling for the non-steady state approach is

conducted in a Lagrangian framework. The changes in thorium activity within an eddy are more likely to represent the temporal evolution of the water mass. Unfortunately, eddies vary strongly in their coherency and their boundaries do not prevent all dynamical exchanges of thorium with the surrounding waters, as is apparent in our case study. It is extremely difficult to evaluate the "permeability" of an eddy in a model, and much more so in the field, so the accuracy of the Lagrangian non-steady state approach remains difficult to estimate.

This study emphasizes that errors associated either with the sampling method (sampling density, Eulerian vs. Lagrangian) or the thorium model (steady state, non-steady state) vary spatially with the eddy kinetic energy and the productivity. It is, however, worth noting that they also vary seasonally. They are smallest in post-bloom conditions (late summer and fall), when the export and, hence, its spatial variability are low, and increase by a third when the bloom and the thorium flux peak (spring to early summer). Succinctly, they are largest when the flux is largest and of most interest.

7. Conclusion

The first part of this work was dedicated to the exploring of small-scale spatial variability of particle export in the north Atlantic, using surface and subsurface thorium observations. Significant spatial variability of the order of 100-1000 $dpm.m^{-2}.d^{-1}$ over spatial scales of 100 km and smaller was demonstrated, in agreement with the previous observational study of Buesseler et al. (2009). Regions of highest patchiness are associated with high eddy kinetic energy and/or high productivity. The second aspect of this study focused on how this spatial variability at small-scales impacts the estimation of export derived from thorium observations. Results from a physical-biogeochemical model resolving small spatial scales highlighted three main sources of bias associated with the fact that most thorium-based estimations implicitly assume that there is no patchiness in thorium activity and export. We found that the primary source of error in thorium-based export estimates associated with the presence of small-scale spatial variability is related to the standard assumptions of steady state and non-steady state (>40%). The second largest errors (>20%) can be attributed to the undersampling of this patchiness. In contrast, we found that errors due to the dynamical transport of thorium associated with small-scale structures are relatively low (<20%) except in regions of high eddy kinetic energy such as boundary currents.

The reader should keep in mind that the estimated errors on the thorium export flux were derived from a particular model setting, which is likely to influence the magnitude of these errors. The physical and biogeochemical models used here are idealised in many ways. The idealised geometry of the domain, the absence of topography and the simple wind forcing hinder direct comparison with the real ocean. The simple structure of the ecosystem (one phytoplankton, one zooplankton and two detritus size classes) and the assumptions underlying some of the thorium dynamics (such as the constant adsorption constant) limit the model's ability to reproduce the wide range of ecosystems and carbon to thorium ratios that are observed in-situ. In addition, the model estimated errors represent the worse case scenario in the model; they were computed using the 95% confidence interval, which means that the difference between the estimated thorium flux and the calculated thorium flux will generally be lower or equal to the model-derived error, particularly in regions and periods of low export flux. Error estimates for other means of estimating export are still far from reliable or thorough, and so care should be exercised in comparing the errors for thorium measurements discussed here and those derived from observations. Nevertheless, these results can be used to assess the relative size of errors in the different way that thorium measurements could be conducted and hopefully provide strong practical assistence to improve the accuracy of field measurements.

We have demonstrated that the estimation of thorium export depends on the spatial variability of thorium activity. We therefore recommend a thorough assessment of this spatial variability either directly, using observations of thorium activity at relatively high resolution (as performed by Buesseler et al., 2009 and in the cruise presented in this study), or indirectly, using eddy kinetic energy and the surface chlorophyll concentration derived from satellite observations, shown here to be good proxies. Another substantial finding is that the widely observed lack of correlation between phytoplankton-related fields and particle export estimated from thorium could be explained by the different time scales at which thorium scavenging, phytoplankton and particle export flux vary. In the real ocean, processes not represented in the biogeochemical model could further modulate this effect. Indeed, the model does not represent the spatial variability of export and remineralisation introduced by mechanisms other than ocean physics, such as the ecosystem assemblage, ballasting effects etc. However, it should be kept in mind that although the patchiness in thorium and the entanglement of spatial and temporal scales complicate the estimation of particle export from thorium measurements, other methods used to estimate particle export, such as sediment traps

or nutrient budgets, do not necessarily provide estimates with better spatial coverage and may hence suffer from errors whose magnitude needs to be assessed.

Acknowledgements

We sincerely thank K. Buesseler and two anonymous reviewers for their comments on this paper. This work was funded by a grant from Eur-Oceans as part of their flagship, 'The influence of mesoscale and sub-mesoscale ocean dynamics on the global carbon cycle and marine ecosystems'. We thank the NEMO team in Paris and Southampton for developing, maintaining and providing assistance with the NEMO ocean general circulation model. We are grateful to the scientists, technicians, officers and crew on RRS Discovery cruise 341 who made the collection of this data possible and to the NERC funded Oceans 2025 project under which these cruises were carried out. The Chlorophyll data were provided by the SeaWiFS Project and NASA's DAAC. Sea surface temperatures have been constructed operationally from the five-channel AVHRR by NOAA's National Environmental Satellite, Data, and Information Service (NESDIS). The altimeter products were produced by Ssalto/Duacs and distributed by Aviso with support from CNES.

References

Abraham, E. R. (1998). The generation of plankton patchiness by turbulent stirring, Nature, 391, 577–580, 1998.

Abraham, E. R., C. S. Law, P. W. Boyd, S. J. Lavender, M. T. Mal- donado and A. R. Bowie (2000). Importance of stirring in the development of an iron-fertilized phytoplankton bloom, Nature, 407, 727.

Allen, J., T., L. Brown, R. Sanders, C. M. Moore, A. Mustard, S. Fielding, M. Lucas, M. Rixen, G. Savage, S. Henson and D. Mayor (2005). Diatom carbon export enhanced by silicate upwelling in the northeast Atlantic. Nature, 437, (7059), 728-732.

Alonso-González, I. J., Arístegui, J., Lee, C., and Calafat, A. (2010). Regional and temporal variability of sinking organic matter in the subtropical northeast Atlantic Ocean: a biomarker diagnosis, Biogeosciences, 7, 2101-2115, doi:10.5194/bg-7-2101-2010.

Aumont, O., E. Maier-Reimer, S. Blain, and P. Monfray (2003). An ecosystem model of the global ocean including Fe, Si, P co-limitation, Global Biogeochem. Cycles, 17, 1060, doi: 10.1029/2001GB001745.

Bacon, M., P., and R. F. Anderson (1982). Distribution of thorium isotopes between dissolved and particulate forms in the deep sea. Journal of Geophysical Research 87, 2045–2056.

Bacon M., P., J. K. Cochran, D. Hirschberg, T. R. Hammar and A. P. Fleer (1996). Export flux of carbon at the equator during the EqPac time-series cruises estimated from ^{234}Th measurements. Deep-Sea Research II, 43 (4-6), 1133-1153.

Beaulieu, S. E. (2002). Accumulation and fate of phytodetritus on the sea floor. Oceanogr. Mar. Biol. 40: 171–232.

Benitez-Nelson, C.R., K. O.Buesseler and G. Crossin (2000) Upper ocean carbon export, eddy diffusivity and horizontal transport in the southwestern Gulf of Maine. *Cont. Shelf Res.*, 20, 707-736.

Benitez-Nelson, C. R., R. R. Bidigare, T. D. Dickey, M. R. Landry, C. L. Leonard, S. L. Brown, F. Nencioli, Y. M. Rii, K. Maiti, J. W. Becker, T. S. Bibby, W. Black, W.-J. Cai, C. A. Carlson, F. Chen, V. S. Kuwahara, C. Mahaffey, P. M. McAndrew, P. D. Quay, M. S. Rappé, K. E. Selph, M. P. Simmons, and E. Jin Yang (2007). Mesoscale Eddies Drive Increased Silica Export in the Subtropical Pacific Ocean. Science: 316 (5827), 1017-1021, doi:10.1126/science.1136221.

Benitez-Nelson C., R., and D. J. McGillicuddy Jr. (2008). Mesoscale physical-biological-biogeochemical linkages in the open ocean: An introduction to the results of the E-Flux and EDDIES programs, Deep Sea Research Part II: Topical Studies in Oceanography, 55(10-13), 1133-1138, doi:10.1016/j.dsr2.2008.03.001.

Berelson, W. M. (2002), Particle settling rates increase with depth in the ocean, Deep Sea Res. Part II, 49, 237–251.

Bishop, J.K.B., T.J. Wood, R.E Davis, J.T. Sherman (2004). Robotic Observations of Enhanced Carbon Biomass and Carbon Export at 55S During SOFeX - Science, 304, 417-420, doi:10.1126/science.1087717.

Boyd, P.W., Sherry, N.D., Berges, J.A., Bishop, J.K.B., Calvert, S.E., Charette, M.A., Giovannoni, S.J., Goldblatt, R., Harrison, P.J., Moran, S.B., Roy, S., Soon, M., Strom, S., (1999). Transformations of biogenic particulates from the pelagic to the deep ocean realm. Deep-Sea Research Part II 46 (11–12), 2761–2792.

Buesseler, K.O., (1991). Do upper-ocean sediment traps provide an accurate record of particle flux? Nature 353, 420–423.

Buesseler, K.O., Bacon, M.P., Cochran, J.K., Livingston, H.D., (1992). Carbon and nitrogen export during the JGOFS North Atlantic bloom experiment estimated from 234Th:238U disequilibria. Deep-Sea Research 39 (7/8), 1115–1137.

Buesseler, K. O., J. A. Andrews, R. Belastock, and F. Chai, (1995). Regional estimates of the export flux of particulate organic carbon derived from thorium-234 during the JGOFS EQPAC program. *Deep-Sea Research II* 42(2-3): 777-804.

Buesseler, K. O., L. Ball, J. A. Andrews, C. R. Benitez-Nelson, R. Belastock, F. Chai, and Y. Chao (1998). Upper ocean export of particulate organic carbon in the Arabian Sea derived from thorium-234. *Deep-Sea Research II* 45(10-11): 2461-2487.

Buesseler, K.O., Benitez-Nelson, C.R., Moran, S.B., Burd, A., Charette, M., Cochran, J.K., Coppola, L., Fisher, N.S., Fowler, S.W., Gardner, W.D., Guo, L.D., Gustafsson, O., Lamborg, C., Masque, P., Miquel, J.C., Passow, U., Santschi, P.H., Savoye, N., Stewart, G., Trull, T., (2006). An assessment of particulate organic carbon to thorium-234 ratios in the ocean and their impact on the application of 234Th as a POC flux proxy. Marine Chemistry 100, 213–233.

Buesseler, K.O., Antia, A.N., Chen, M., Fowler, S.W., Gardner, W.D., Gustaffson, Ö., Harada, K., Michaels, A.F., Rutgers van der Loeff, M., Sarin, M., Steinberg, D.K., Trull, T., (2007). An assessment of the use of sediment traps for estimating upper ocean particle fluxes. Journal of Marine Research 65, 345–416.

Buesseler, K.,O., C. Lamborg, P. Cai, R. Escoube, R. Johnson, S. Pike, P. Masque, D. McGillicuddy, E. Verdeny (2008). Particle fluxes associated with mesoscale eddies in the Sargasso Sea, Deep Sea Research Part II: Topical Studies in Oceanography, Volume 55, Issues 10-13, 1426-1444, ISSN 0967-0645, 10.1016/j.dsr2.2008.02.007.

Buesseler, K.,O., S. Pike, K. Maiti, C.H. Lamborg, D.A. Siegel, T.W. Trull, Thorium-234 as a tracer of spatial, temporal and vertical variability in particle flux in the North Pacific, Deep Sea Research Part I: Oceanographic Research Papers, Volume 56, Issue 7, 1143-1167, ISSN 0967-0637, 10.1016/j.dsr.2009.04.001.

Charette, M. A., S. B. Moran, S. M. Pike and J. N. Smith (2001). Investigating the carbon cycle in the Gulf of Maine using natural tracer thorium-234. Journal of Geophysical Research, 106 (C6), 11, 553-579.

Chen, J.H., Edwards, R.L., Wasserburg, G.J. (1986). 238U, 234U and 232Th in seawater. Earth and Planetary Science Letters 80, 241–251.

Clegg, S.L., Whitfield, M., (1993). Application of a generalized scav- enging model to time series 234Th and particle data collected during the JGOFS North Atlantic Bloom Experiment. Deep-Sea Research I, 40, 1529–1545.

Clegg, S.L., Bacon, M.P., Whitfield, M., (1991). Application of a generalized scavenging model to thorium isotope and particle data at equatorial and high-latitude sites in the Pacific Ocean. Journal of Geophysical Research 96, 20655–20670.

Cochran, J.K., Buesseler, K.O., Bacon, M.P. and Livingston, H.D. (1993). Thorium isotopes as indicator of particle dynamics in the upper ocean: results from the JGOFS North Atlantic Bloom Experiment. Deep-Sea Research I, 40, 1569–1595.

Cochran, J.K., Masqué, P., (2003). Short-lived U / Th series radio-nuclides in the ocean: tracers for scavenging rates, export fluxes and particle dynamics. In: Bourdon, B., Henderson, G.M., Lundstrom, C.C., Turner, S.P. (Eds.), Uranium-Series Geochemistry, Reviews in Mineralogy and Geochemistry, vol. 52, pp. 461–492.

Dunne, J.P., Murray, J.W., Young, J., Balistrieri, L.S., Bishop, J., (1997). ^{234}Th and particle cycling in the central equatorial Pacific. Deep-Sea Research II, 44, 2049–2083.

Dunne, J.P. and J. W. Murray (1999). Sensitivity of ^{234}Th export to physical processes in the central equatorial Pacific. Deep-Sea Research I, 46, 831-854.

Fielding, S., Crisp, N., Allen, J.T., Hartman, M.C., Rabe, B. and Roe, H.S.J. (2001). Mesoscale subduction at the Almeria-Oran front. Part 2: biophysical interactions. Journal of Marine Systems, 30, (3-4), 287-304, doi:10.1016/S0924-7963(01)00063-X

Gehlen, M., Bopp, L., Emprin, N., Aumont, O., Heinze, C., and Ragueneau, O. (2006). Reconciling surface ocean productivity, export fluxes and sediment composition in a global biogeochemical ocean model, Biogeosciences, 3, 521-537, doi:10.5194/bg-3-521-2006.

Guidi, L., L. Stemmann, L. Legendre, M. Picheral, L. Prieur, and G. Gorsky, (2007). Vertical distribution of aggregates (> 110 μm) and mesoscale activity in the northeastern Atlantic: Effects on the deep vertical export of surface carbon. Limnol. Oceanogr. 52: 7-18.

Gustafsson, Ö, K. O. Buesseler, W. R. Geyer, S. B. Moran and P. M. Gschwend (1998). An assessment of the relative importance of horizontal and vertical transport of particle reactive chemicals in the coastal ocean. Continental Shelf Research, 18, 805-829.

Hernández-Garcia, E.,C. López, and Z. Neufeld (2002): Small-scale structure of nonlinearly interacting species advected by chaotic flows, Chaos, 12, 470.

Honeyman, B.D., Balistrieri, L.S., Murray, J.W., (1988). Oceanic trace metal scavenging: the importance of particle concentration. Deep-Sea Res. Part I, 35, 227–246.

Honjo, S., J. Dymond, W. Prell, and V. Ittekkot (1999), Monsoon-controlled export fluxes to the interior of the Arabian Sea, Deep Sea Research Part II: Topical Studies in Oceanography, 46 (8-9), 1859-1902, doi:doi: 10.1016/S0967-0645(99)00047-8.

Jenkins, W.J., 1982. Oxygen utilization rates in north-atlantic sub-tropical gyre and primary production in oligotrophic systems. Nature, 300 (5889), 246–248.

Karleskind, P., M. Lévy and L. Mémery (2011). Subduction of carbon, oxygen and nitrogen in the Northeast Atlantic, J. Geophys. Res., 116, C02025, doi:10.1029/2010JC006446

Klein, P., A.-M. Tréguier and B. L. Hua (1998): Three-dimensional stirring of thermohaline fronts, J. Mar. Res., 56, 589-612.

Kremeur, A.-S., M. Lévy, O. Aumont and G. Reverdin (2009). Impact of the subtropical mode water biogeochemical properties on primary production in the North Atlantic: new insights from an idealized model study, J. Geophys. Res., 114, C07019, doi:10.1029/2008JC005161.

Kriest, I. (2002), Different parameterizations of marine snow in a 1-D model and their influence on representation of marine snow, nitrogen budget and sedimentation, Deep Sea Res. Part I, 49, 2133–2162.

Lampitt, R.S., Achterberg, E.P., Anderson, T.R., Hughes, J.A., Iglesias-Rodriguez, M.D., Kelly-Gerreyn, B.A., Lucas, M., Popova, E.E., Sanders, R., Shepherd, J.G., Smythe-Wright, D. and Yool, A. (2008) Ocean fertilisation: a potential means of geo-engineering? Philosophical Transactions of the Royal Society A, 366, (1882), 3919-3945. (doi:10.1098/rsta.2008.0139)

Lathuilière, C., V. Echevin, M. Lévy and G. Madec, On the role of mesoscale circulation on an idealized coastal upwelling ecosystem (2010), J. Geophys. Res., Vol 115, C09018, doi:10.1029/2009JC005827

Le Moigne, F.A.C., M. Villa, R.J. Sanders, C. Marsay, S. Henson and R. García-Tenorio. Insights from POC and biominerals ^{234}Th and ^{210}Po derived export study at the Porcupine Abyssal Plain: Implications for the ballast hypothesis. In review In Deep Sea Res. Part I.

Lévy, M, Klein, P. and A.-M. Treguier (2001). Impacts of submesoscale physics on phytoplankton production and subduction, J. Mar. Res., 59,535-565 doi: 10.1357/002224001762842181

Lévy, M. and P. Klein (2004). Does the low frequency variability of mesoscale dynamics explain a part of the phytoplankton and zooplankton spectral variability ? Proc. Royal Soc. Lon., 460, 1673-1683.

Lévy, M. (2008). The modulation of biological production by oceanic mesoscal turbulence, Lect. Notes Phys., 744, 219-261, DOI 10.1007/978-3-540-75215-8_9, Transport in Geophysical flow: Ten years after, J. B. Weiss and A. Provenzale (Eds), Springler

Lévy, M., P. Klein, A.-M. Tréguier, D. Iovino, G. Madec, S. Masson and K. Takahashi (2010). Modifications of gyre circulation by submesoscale physics, Ocean Modelling, doi:10.1016/j.ocemod.2010.04.001, 34, 1-15

Lévy, M., L. Resplandy, P. Klein, X. Capet and C. Ethé (2012a). Grid degradation of submesoscale resolving ocean models: benefits for offline tracer transport, Ocean Modelling, in press.

Lévy, M., D. Iovino, L. Resplandy, P. Klein, A.-M. Tréguier, G. Madec, S. Masson and K. Takahashi (2012b). Large-scale impacts of submesoscale dynamics on phytoplankton : local and remote effects, Ocean Modelling, vol 43-44, 77-93, doi:10.1016/j.ocemod.2011.12.003.

Lévy, M., R. Ferrari, P. Franks, A. Martin and P. Rivière, Bringing physics to life at the submesoscale, in revision for GRL.

Madec G. 2008: NEMO ocean engine. Note du Pole de modélisation, Institut Pierre-Simon Laplace (IPSL), France, No 27 ISSN No 1288-1619. Available online: www.nemo-ocean.eu/About-NEMO/Reference-manuals.

Maiti K., C. R. Benitez-Nelson, Y. Rii and R. Bidigare, The influence of a mature cyclonic eddy on particle export in the lee of Hawaii, Deep Sea Research Part II: Topical Studies in Oceanography, Volume 55, Issues 10-13, May-June 2008, Pages 1445-1460, ISSN 0967-0645, 10.1016/j.dsr2.2008.02.008.

Martin, A.P., Richards, K.J. and Fasham, M.J.R. (2001). Phytoplankton production and community structure in an unstable frontal region. Journal of Marine Systems, 28, (1-2), 65-89, doi: 10.1016/S0924-7963(00)00084-1.

Martin, A.P. and Srokosz, M.A. (2002) Plankton distribution spectra: inter-size class variability and the relative slopes for phytoplankton and zooplankton. Geophysical Research Letters, 29, (24), art.2213. (doi:10.1029/2002GL015117)

Martin, A.P. (2003). Phytoplankton patchiness: the role of lateral stirring and mixing. Progress in Oceanography, 57, (2), 125-174, doi:10.1016/S0079-6611(03)00085-5.

Martin P., Richard S. Lampitt, Mary Jane Perry, Richard Sanders, Craig Lee, Eric D'Asaro, Export and mesopelagic particle flux during a North Atlantic spring diatom bloom, Deep Sea Research Part I: Oceanographic Research Papers, Volume 58, Issue 4, 2011, Pages 338-349, ISSN 0967-0637, 10.1016/j.dsr.2011.01.006.

Martinez, E. and Richards, K.J. (2010). Impact of spatio-temporal heterogeneities and lateral stirring and mixing on midwater biotic interactions. Journal of Marine Systems, 82, 122–134.

McGillicuddy, D.J., Anderson, L.A., Bates, N.R., Bibby, T., Buesseler, K.O., Carlson, C.A., Davis, C.S., Ewart, C., Falkowski, P.G., Goldthwait, S.A., Hansell, D.A., Jenkins, W.J., Johnson, R., Kosnyrev, V.K., Ledwell, J.R., Li, Q.P., Siegel, D.A. and D.K. Steinberg, (2007). Eddy/Wind Interactions Stimulate Extraordinary Mid-Ocean Plankton Blooms. Science, **316**, 1021-1026.

Murnane, R.J., Cochran, J.K., Sarmiento, J.L. (1994). Estimates of particle- and thorium-cycling rates in the northwest Atlantic Ocean. Journal of Geophysical Research 99, 3373–3392.

Murnane, R.J., Cochran, K.O. Buesseler and M.P. Bacon (1996). Least-squares estimates of thorium, particle, and nutrient cycling rate constants from the JGOFS North Atlantic Bloom Experiment. Deep-Sea Research I, 43(2), 238–258.

Morris, P.J., Sanders, R., Turnewitsch, R., Thomalla, S. (2007). 234Th-derived particulate organic carbon export from an island-induced phyto- plankton bloom in the Southern Ocean. Deep-Sea Research II 54, 2208–2232.

Neufeld, Z., C. López, and P. H. Haynes (1999): Smooth-filamental transition of active tracer fields stirred by chaotic advection, Phys. Rev. Lett. 82, 2606.

Newton P.P., Lampitt R.S., Jickells T.D., King P. and Boutle C., 1994, Temporal and spatial variability of biogenic particle fluxes during the JGOFS northeast Atlantic process studies at 47N 20W. Deep-Sea Research I, 41: 1617-1642.

Nodder, S. D., and L. C. Northcote (2001). Episodic particulate fluxes at southern temperate mid-latitudes (42–45 degrees S) in the Subtropical Front region, east of New Zealand. Deep-Sea Res. I, 48: 833–864.

d'Ovidio, F., S. De Monte, S. Alvain, Y. Dandonneau and M. Lévy (2010), Fluid dynamical niches of phytoplankton types, PNAS, 107 (43) 18366-18370, doi/10.1073/pnas.1004620107.

Painter, Stuart C., Pidcock, Rosalind E. and Allen, John T. (2010) A mesoscale eddy driving spatial and temporal heterogeneity in the productivity of the euphotic zone of the northeast Atlantic. Deep Sea Research Part II: Topical Studies in Oceanography, 57, (15), 1281-1292. (doi:10.1016/j.dsr2.2010.01.005).

Plattner, G.-K., N. Gruber, H. Frenzel, and J. C. McWilliams (2005). Decoupling marine export production from new production. Geophysical Research Letters, 32, doi:10.1029/2005GL022660.

Resplandy, L., Lévy, M., d'Ovidio, F. and Merlivat, L. (2009). Impact of submesoscale variability in estimating the air-sea CO2 exchange : Results from a model study of the POMME experiment. Glob. Biogeochem. Cyc., 23. doi :10.1029/2008GB003239.

Rutgers van der Loeff, M., Sarin, M.M., Baskaran, M., Benitez-Nelson, C., Buesseler, K.O., Charette, M., Dai, M., Gustafsson, Ö., Masque, P., Morris, P.J., Orlandini, K., Rodriguez y Baena, A., Savoye, N., Schmidt, S., Turnewitsch, R., Vöge, I., Waples, J.T., (2006). A review of present techniques and methodological advances in analyzing ^{234}Th in aquatic systems. Marine Chemistry 100, 190–212.

Sanders, R., Brown, L., Henson, S., Lucas, M., (2005). New production in the Irminger Basin during 2002. Journal of Marine Systems 55 (3–4), 291–310.

Sanders, R., P. J. Morris, A. J. Poulton, M. C. Stinchcombe, A. Charalampopoulou, M. I. Lucas, and S. J. Thomalla (2010). Does a ballast effect occur in the surface ocean?, Geophys. Res. Lett., 37, L08602, doi:10.1029/2010GL042574.

Savoye, N., C. Benitez-Nelson, A.B. Burd, J.K. Cochran, M. Charette, K.O. Buesseler, G. Jackson, M. Roy-Barman, S. Schmidt, and M. Elskens (2006) ^{234}Th sorption and export models in the water column: A review. Marine Chemistry, 100, 234-249.

Siegenthaler, U. and J. L. Sarmiento (1993). Atmospheric carbon dioxide and the ocean. Nature 359: 119-125.

Smetacek, A.; Naqvi, S.W.A. The next generation of iron fertilization experiments in the Southern Ocean. Phil. Trans. R. Soc. A : 366; 2008; 3947-3967.

Sweeney, E.N., McGillicuddy, D.J. and K.O. Buesseler, 2003. Biogeochemical impacts due to mesoscale eddy activity in the Sargasso Sea as measured at the Bermuda Atlantic Time Series (BATS) site. Deep-Sea Research II, 50, 3017-3039.

Thomalla, S.,J., Turnewitsch, R., Lucas, M., Poulton, A. (2006). Particulate organic carbon export from the North and South Atlantic: the 234Th/238U disequilibrium approach. Deep-Sea Research II, 53, 1629-1648.

Thomalla S., J., (2007). Particulate organic carbon and minéral export from the North and South Atlantic Gyres : the 234Th/238U disequilibrium approach. University of Capetown. 540pp.

Trull, T.W., S.G. Bray, K.O. Buesseler, C.H. Lamborg, S. Manganini, C. Moy, J. Valdes (2008), In situ measurement of mesopelagic particle sinking rates and the control of carbon transfer to the ocean interior during the Vertical Flux in the Global Ocean (VERTIGO) voyages in the North Pacific, Deep Sea Research Part II: Topical Studies in Oceanography, Volume 55, Issues 14-15, Pages 1684-1695, ISSN 0967-0645, 10.1016/j.dsr2.2008.04.021.

Tsuda, A., Sugisaki, H., Ishimoru, T., Saino, T., and Sato, T.: White-noise-like distribution of the oceanic copepod Neocalanus cristatus in the subarctic North Pacific., Mar. Ecol. Prog. Ser., 97, 39–46, 1993.

Turnewitsch, R. and B. M. Springer (2001): Do bottom mixed layers influence 234Th dynamics in the abyssal near-bottom water column? Deep-sea Research I, 48, 1279-1307, 10.1016/S0967-0637(00)00104-7.

Tzella, A. and P. H. Haynes (2007): Small-scale Spatial Structure in Plankton Distributions,

Biogeosciences, 4, 173-179.

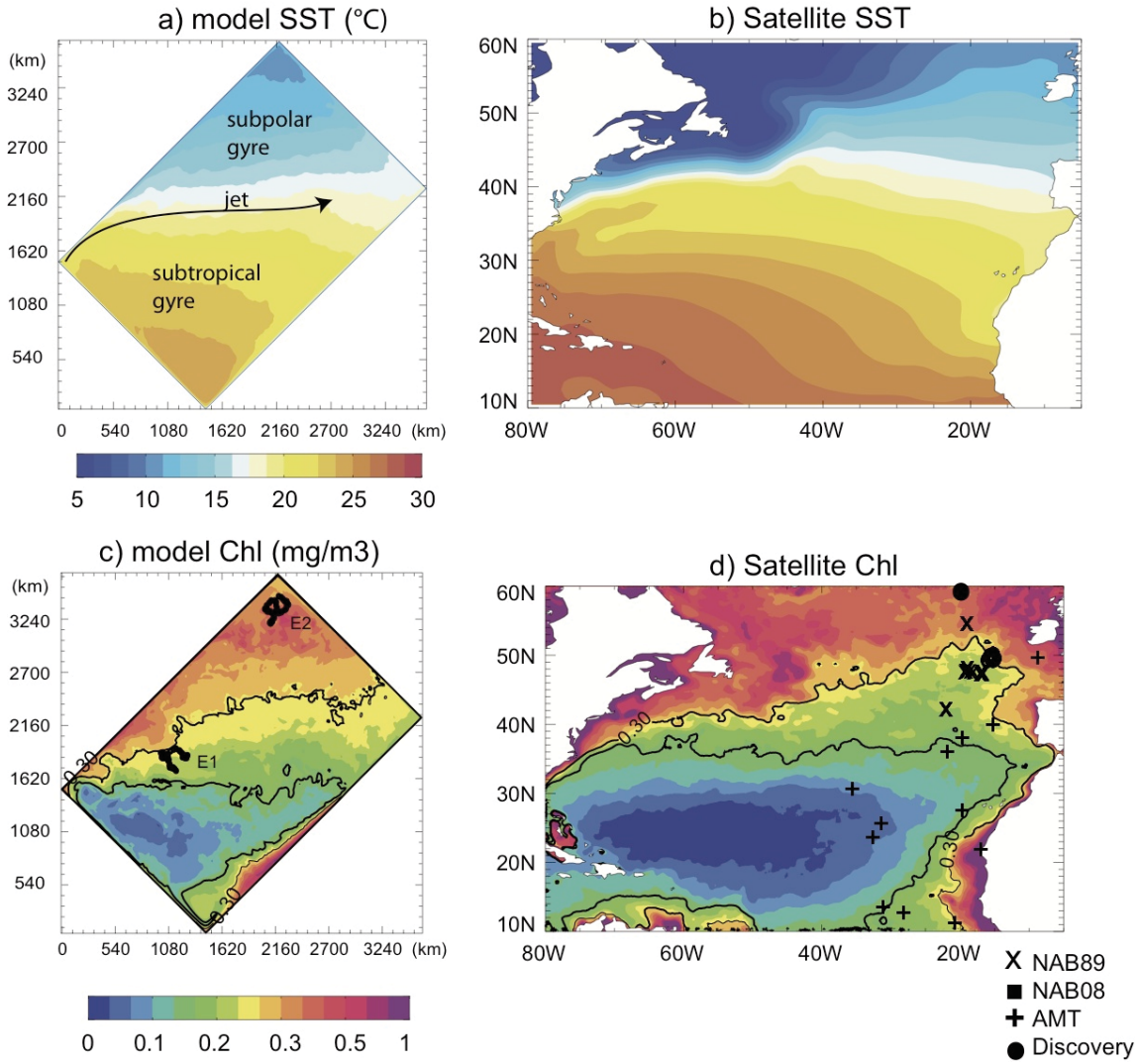

Fig 1: Annual mean sea surface temperature (SST) and surface chlorophyll (Chl) concentration simulated in the model and derived from satellite observations. Arrows on panel a show a schematic representation of the double gyre circulation. Contours on panel c and d delimit the area of Chl concentration equal to 0.15 and 0.3 mg.m^{-3} that are used to delimit the subtropical province, the subpolar province and the transition region. The trajectories of eddies E1 and E2 presented on Fig 11 are indicated on panel c. Symbols on panel d indicate the location of stations used on Fig 3. SST is from satellite AVHRR Oceans Pathfinder and Chl is derived from the ocean color satellite product SeaWiFS.

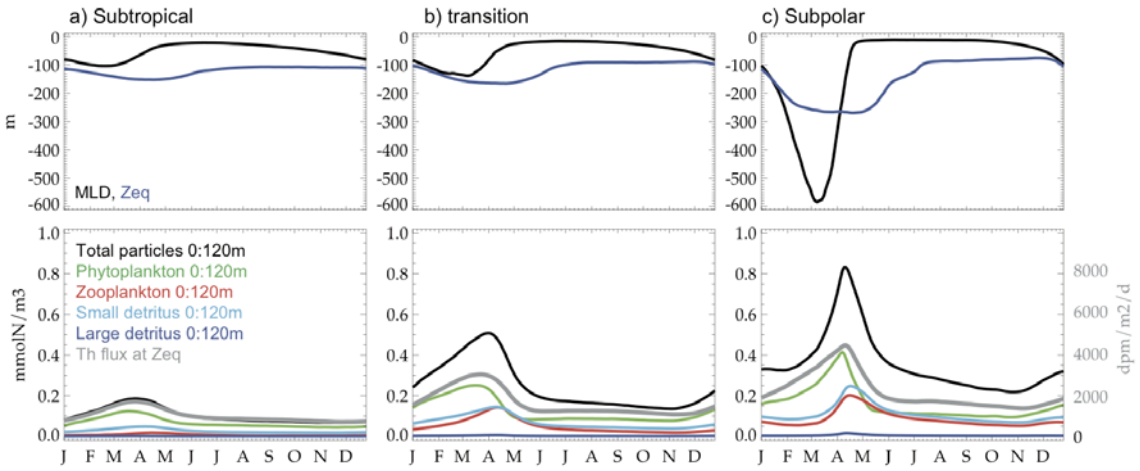

Fig 2: Seasonal cycle of simulated mixed layer depth (MLD, in m), equilibrium depth (Zeq, in m), particles concentrations averaged over the upper 120 m (in mmol N. m^{-3}, total concentration = phytoplankton + zooplankton + small detritus + large detritus) and thorium flux at the equilibrium depth ($dpm.m^{-2}.d^{-1}$) in a) the subtropical province, b) the transition region and c) the subpolar province.

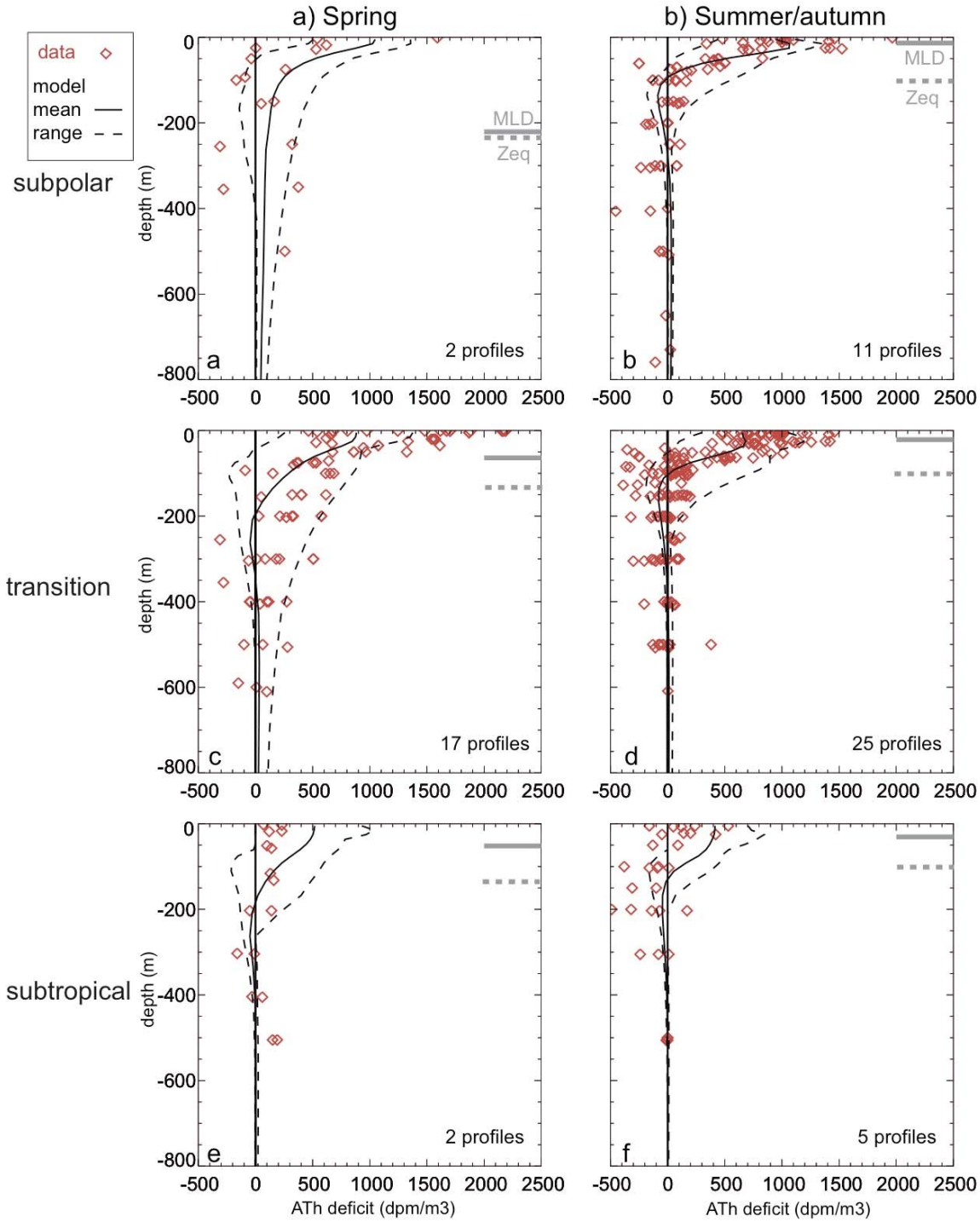

Fig 3: In-situ data and simulated vertical profiles of thorium activity deficit (AU-ATh, in dpm.m^{-3}) in spring (March-May) and summer/autumn (June-September) for the subpolar province, the transition region and the subtropical province. Data are from stations indicated on Fig 1. The number of observed profile used is indicated at the bottom right of each panel. Model mean and range (maximal and minimal values) of ATh deficit are given for each region and season. The grey bars indicate the model mean MLD (solid line) and model mean Zeq (dashed line).

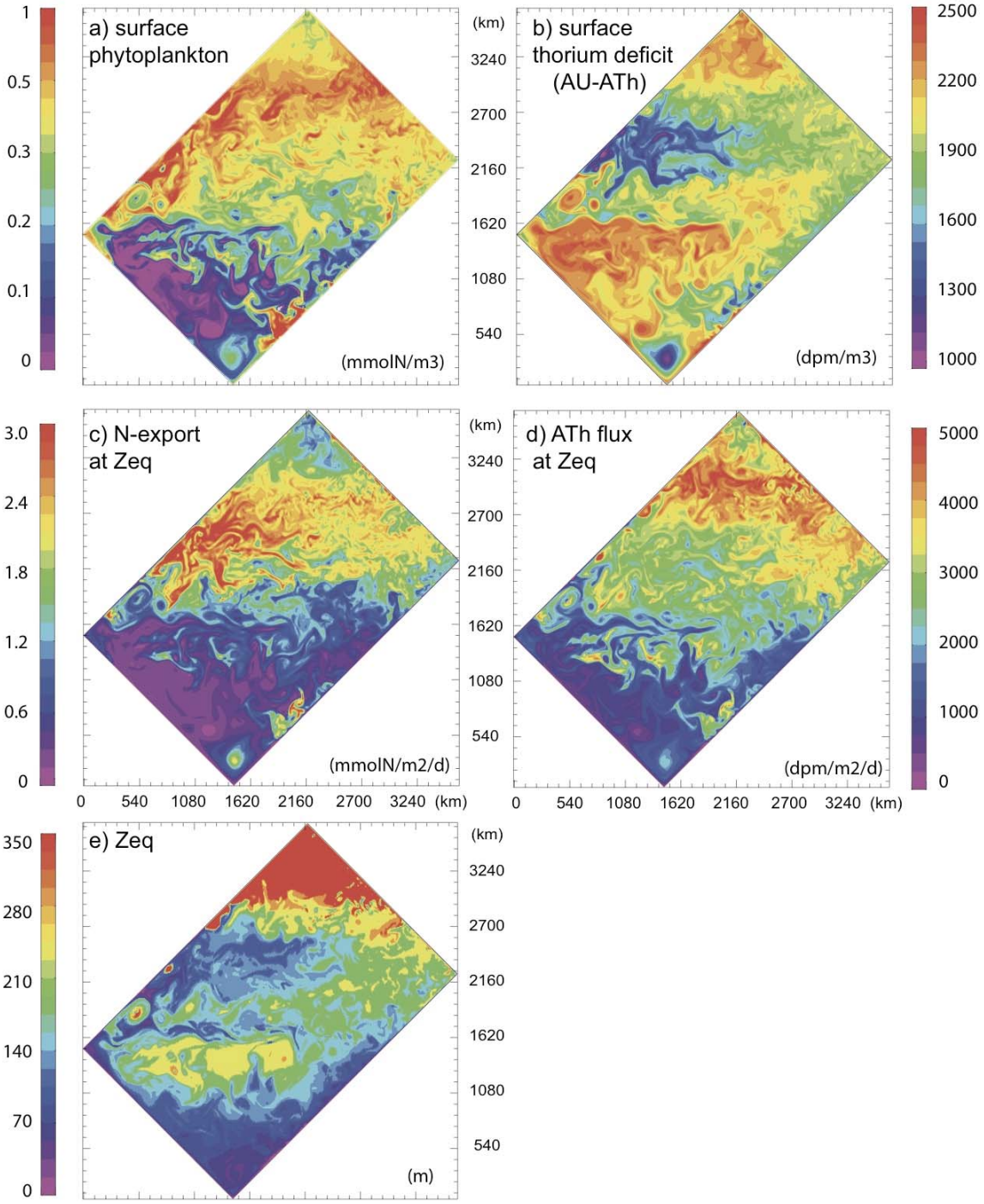

Fig 4: Model snapshots on March 18th: a) sea surface phytoplankton concentration (in mmol $N.m^{-3}$); b) sea surface thorium activity (ATh, in $dpm.m^{-3}$); c) N-export (in mmol $N.m^{-2}.d^{-1}$) at the equilibium depth; d) the thorium flux at the equilibrium depth (in $dpm.m^{-2}.d^{-1}$) and e) Equilibrium depth (Zeq in m).

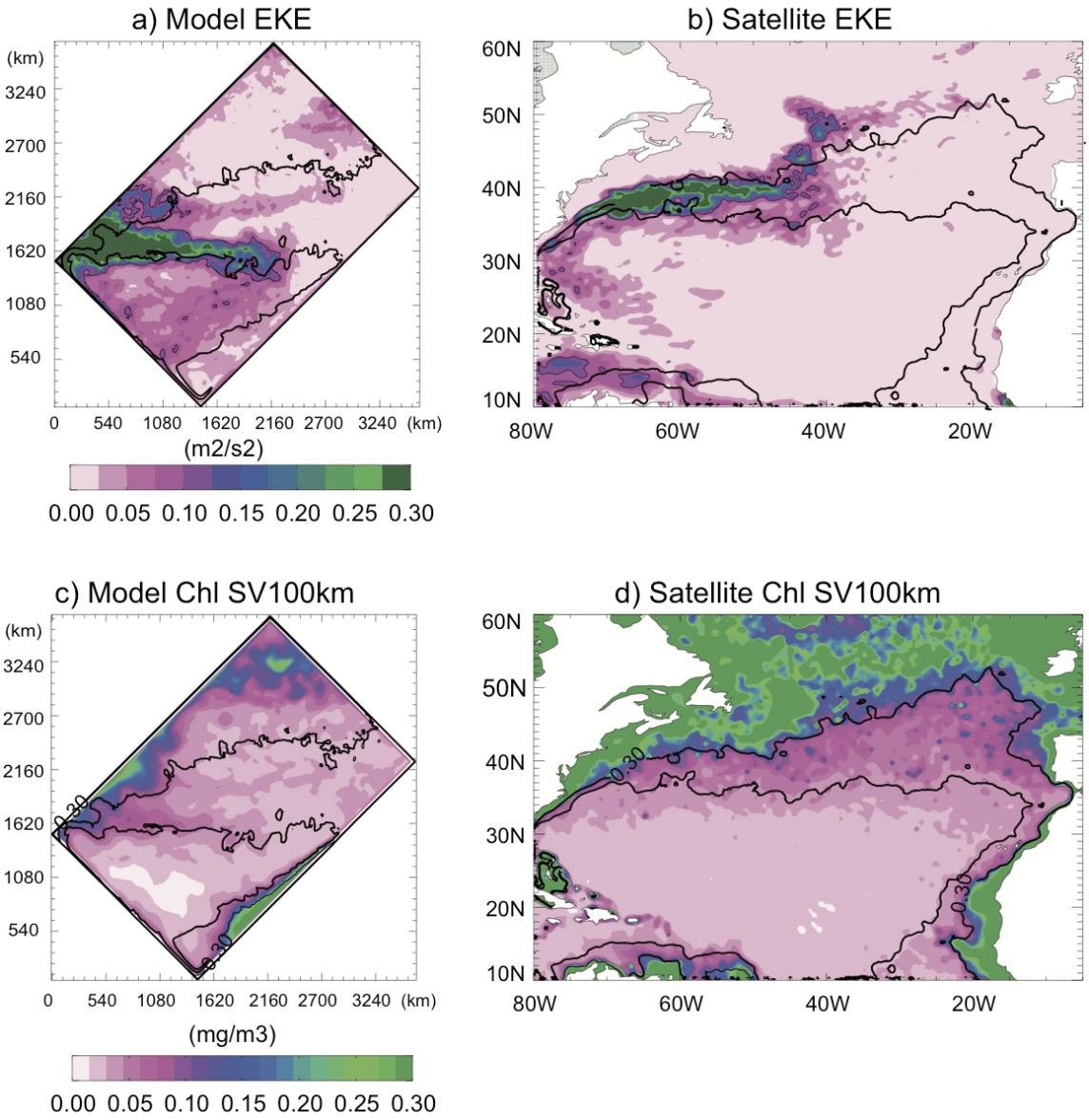

Fig 5: Annual Eddy Kinetic Energy (EKE) calculated from surface annual currents: a) in the model; b) derived from multi-satellite altimetric product Aviso (www.aviso.oceanobs.com). Small-scale spatial variability (SV_{100km}) estimated for surface chlorophyll (Chl) concentration: b) in the model and b) from ocean color satellite product SeaWiFS.

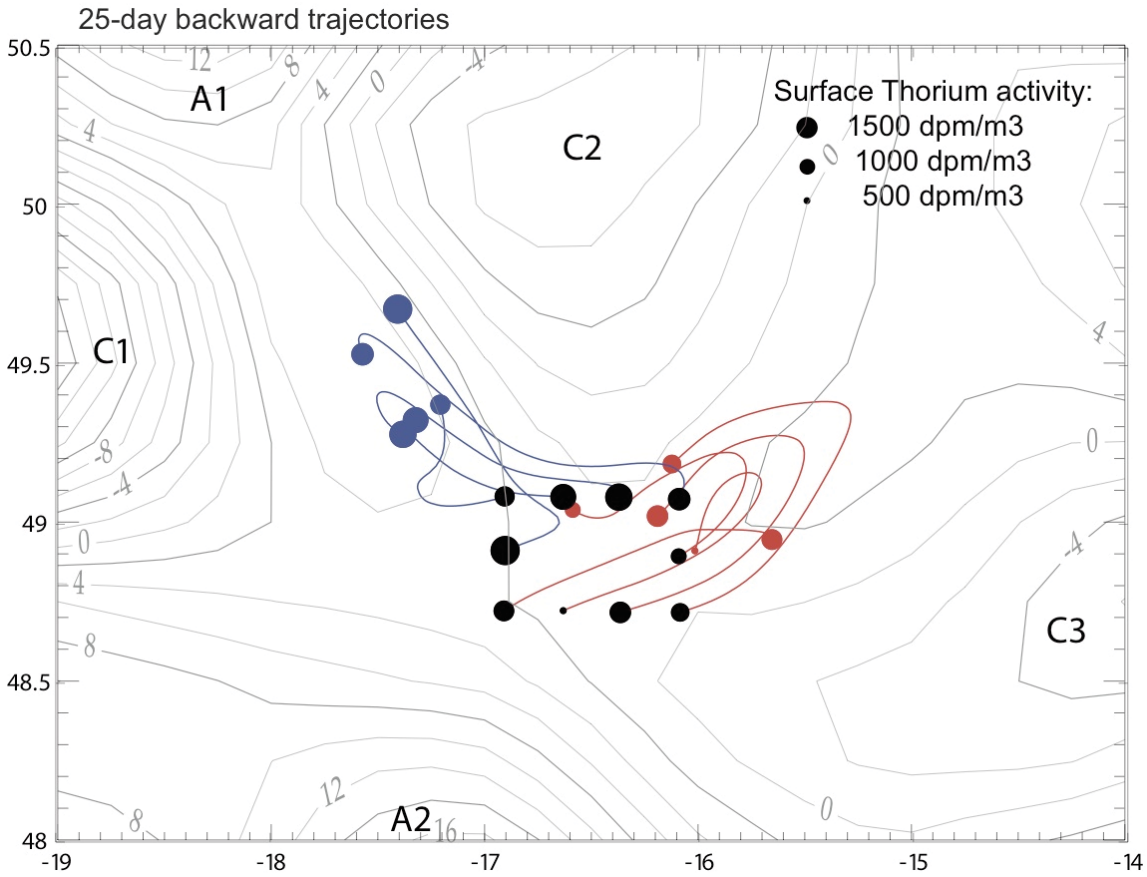

Fig 6: Surface total thorium activity (black circles) sampled at 10 stations around the PAP site (49.5°N, 16.5W) between August, 3rd 17:00 and August, 6th 06:00 in 2009 as part of a NERC-funded UK research cruise on RRS Discovery (D341). Backward trajectories of water parcels located at these 10 stations are computed from the multi-satellite altimetric product Aviso (www.aviso.oceanobs.com, see Resplandy et al. (2009) for details on backward the trajectories calculation). Two clusters of trajectories and the water parcels positions 25 days before the sampling (coloured circles) are identified in blue and red. Sea level anomaly from Aviso on July 15th, 2009 (i.e. during the trajectories) is indicated in grey. Cyclonic and anti-cyclonic eddies are identified by C and A respectively.

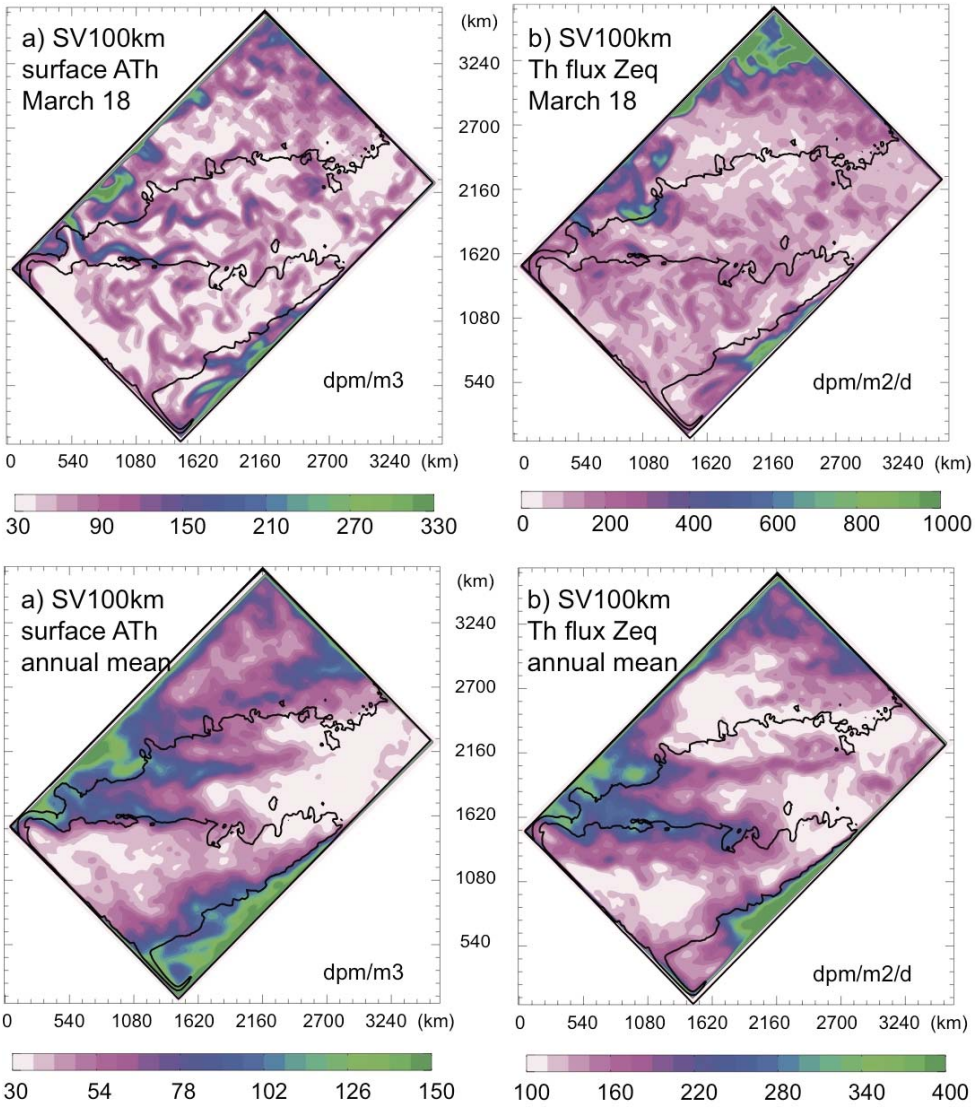

Fig 7: Small-scale spatial variability (SV_{100km}) in the model on the 18th of March (a-b) and annual mean (c-d) for sea surface thorium activity (ATh) and thorium flux at the equilibrium depth.

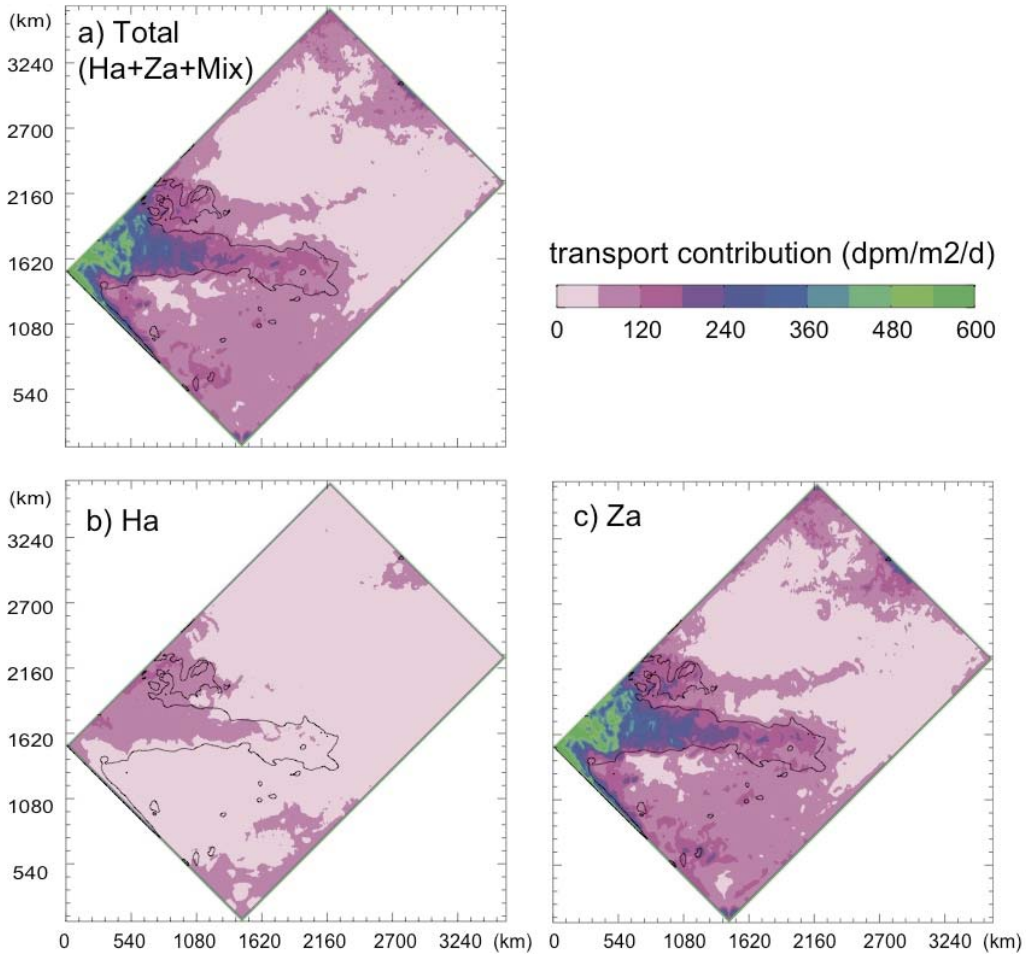

Fig 8: Contribution of the dynamical transport to the thorium budget between the surface and the equilibrium depth (in $dpm.m^{-2}.d^{-1}$): a) total dynamical contribution; b) horizontal advection contribution (Ha) and c) vertical advection contribution (Za).

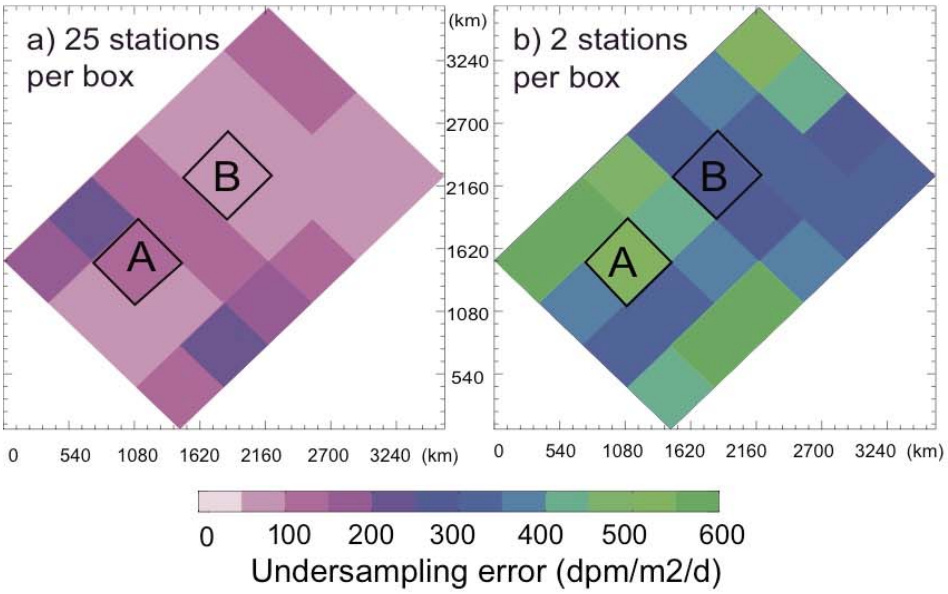

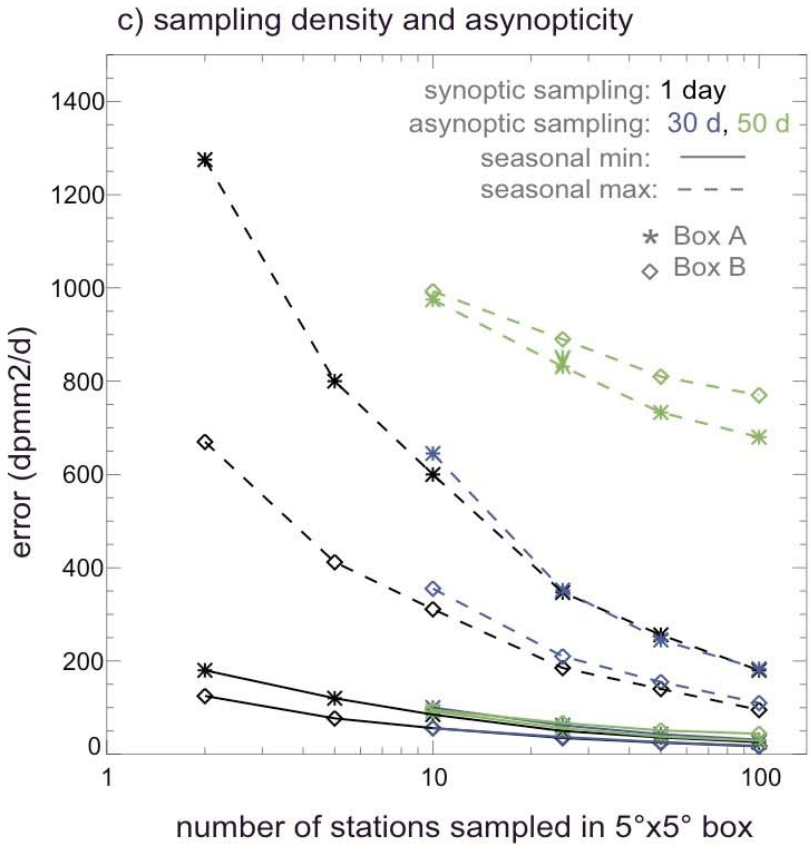

Fig 9: Error on the thorium flux associated with undersampling (in $dpm.m^{-2}.d^{-1}$): a, b) Spatial distribution of the error for synoptic sampling of 25 and 2 stations in each 5°x5° boxes; c) average and maximum error at different sampling resolution (2 to 100 stations) in box A and B (indicated on panel a and b). Results are given for synoptic sampling (black) and asynoptic sampling (30-day, 32-day and 50-day "cruises").

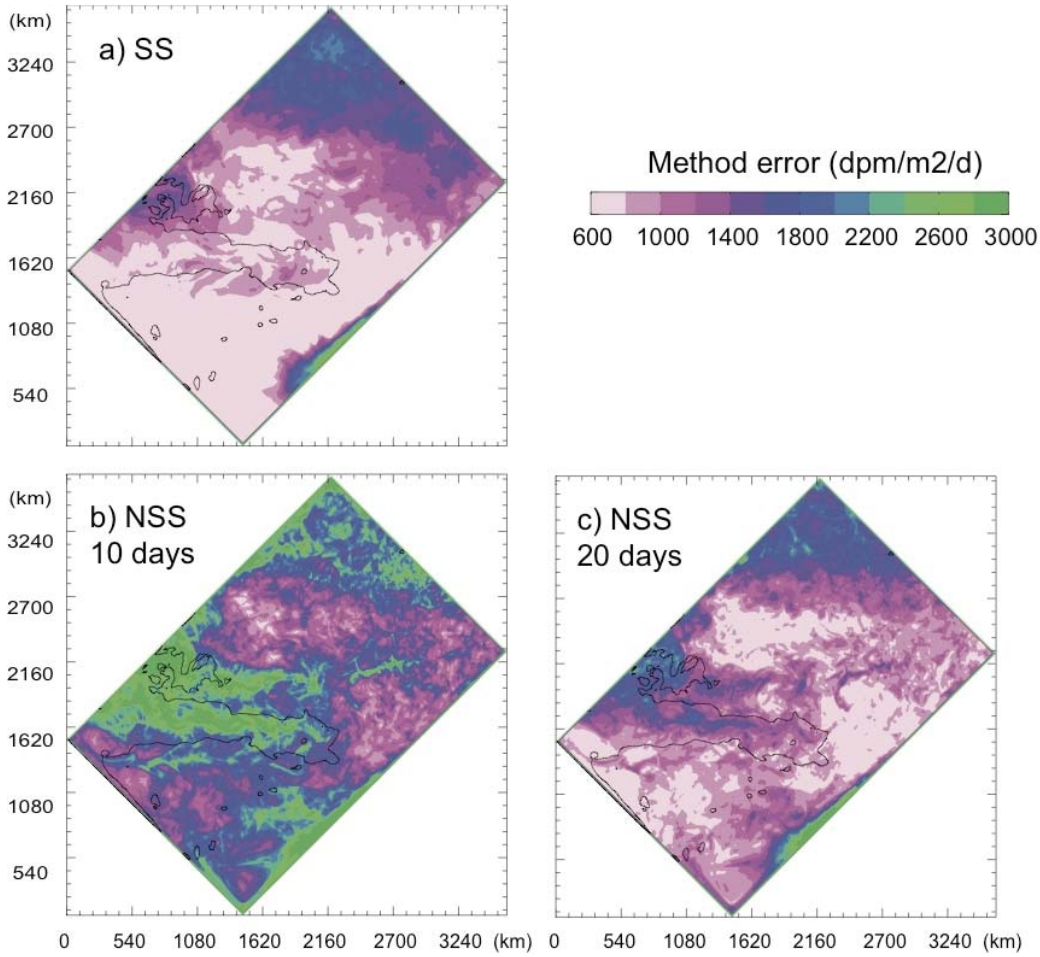

Fig 10: Error on the thorium flux associated with estimation methods (in $dpm.m^{-2}.d^{-1}$): a) steady state approximation (SS); b) and c) non-steady state approximation (NSS) over 10 and 20 days time intervals respectively.

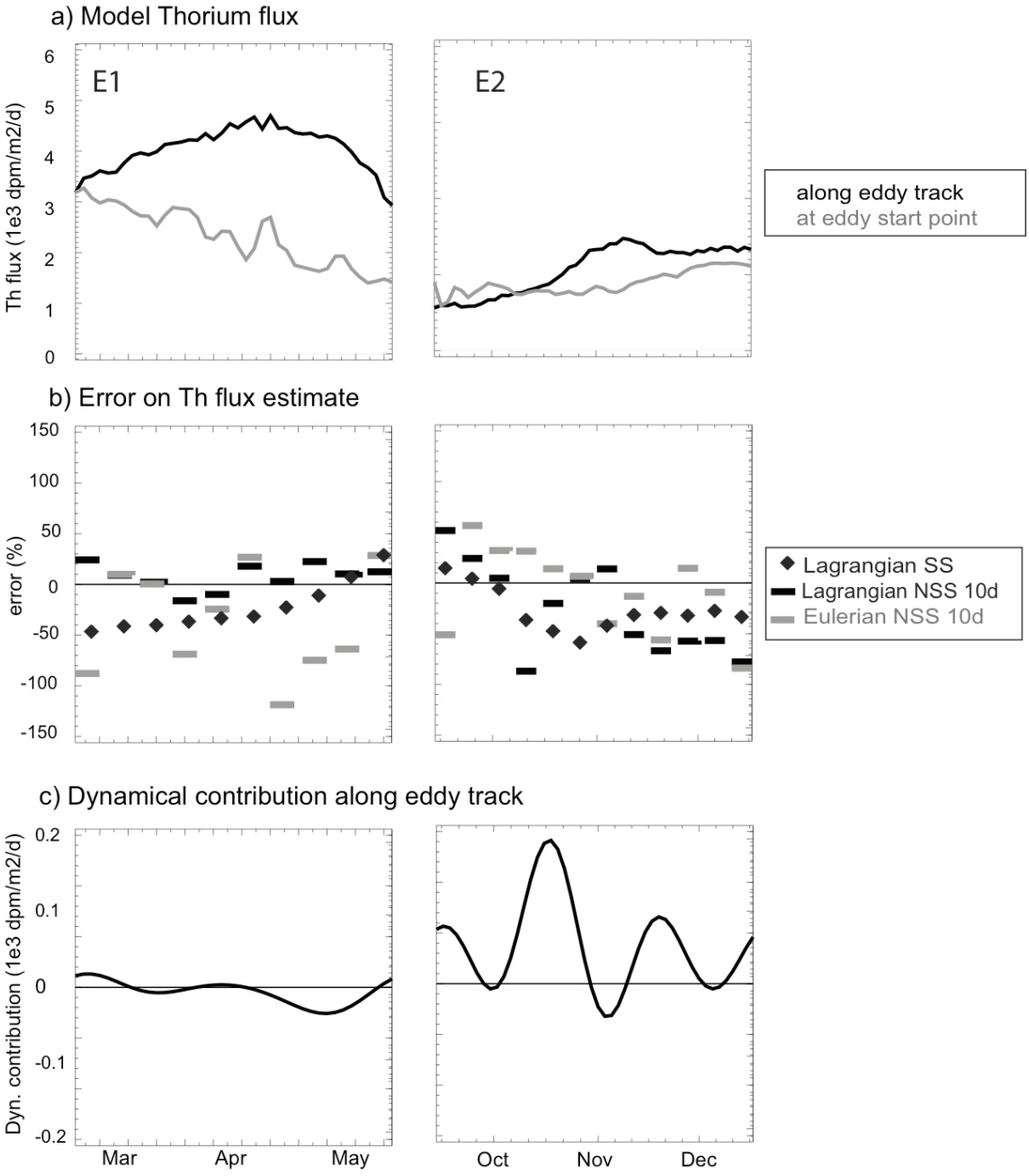

Fig 11: Lagrangian study along the trajectories of eddies E1 (left panels) and E2 (right panels) identified on Fig 1 c: a) Thorium flux predicted by the model along the eddies trajectories (black line) and at the eddy starting point (grey line); b) Error on the flux estimates using the non-steady state approach along the eddy track (black bars) and at the eddy starting point (grey bars) and using the steady state approach along the eddy track (black diamonds); c) Physical transport of thorium at the centre of the eddies.